doi.org/10.26434/chemrxiv.12712106.v1

Controlling Singlet Fission with Coordination Chemistry-Induced Assembly of Dipyridyl Pyrrole Bipentacenes

Ryan Ribson, Gyeongshin Choi, Ryan Hadt, Theodor Agapie

Submitted date: 24/07/2020 • Posted date: 28/07/2020

Citation information: Ribson, Ryan; Choi, Gyeongshin; Hadt, Ryan; Agapie, Theodor (2020): Controlling Singlet Fission with Coordination Chemistry-Induced Assembly of Dipyridyl Pyrrole Bipentacenes. ChemRxiv. Preprint. https://doi.org/10.26434/chemrxiv.12712106.v1

Singlet fission has the potential to surpass current efficiency limits in next-generation photovoltaics and to find use in quantum information science. Despite the demonstration of singlet fission in various materials, there is still a great need for fundamental design principles that allow for tuning of photophysical parameters, including the rate of fission and triplet lifetimes. Here we describe the synthesis and photophysical characterization of a novel bipentacene dipyridyl pyrrole (HDPP-Pent) and its Li- and K-coordinated derivatives. HDPP-Pent undergoes singlet fission at roughly 50% efficiency (τ_{SF} = 730 ps), whereas coordination in the Li complex induces significant structural changes to generate a dimer, resulting in a 5-fold rate increase (τ_{SF} = 140 ps) and near fully efficient singlet fission with virtually no sacrifice in triplet lifetime. We thus illustrate novel design principles to produce favorable singlet fission properties, wherein through-space control can be achieved via coordination chemistry-induced multi-pentacene assembly.

File list (2)

Controlling Singlet Fission with Coordination Chemistry-Induced Assembly of Dipyridyl Pyrrole Bipentacenes

Ryan D. Ribson[1], Gyeongshin Choi[1], Ryan G. Hadt[1]*, Theodor Agapie[1]*

[1]Division of Chemistry and Chemical Engineering, Arthur Amos Noyes Laboratory of Chemical Physics, California Institute of Technology, Pasadena, California 91125, United States* Corresponding authors: rghadt@caltech.edu, agapie@caltech.edu

Singlet fission has the potential to surpass current efficiency limits in next-generation photovoltaics and to find use in quantum information science. Despite the demonstration of singlet fission in various materials, there is still a great need for fundamental design principles that allow for tuning of photophysical parameters, including the rate of fission and triplet lifetimes. Here we describe the synthesis and photophysical characterization of a novel bipentacene dipyridyl pyrrole (HDPP-Pent) and its Li- and K-coordinated derivatives. HDPP-Pent undergoes singlet fission at roughly 50% efficiency (τ_{SF} = 730 ps), whereas coordination in the Li complex induces significant structural changes to generate a dimer, resulting in a 5-fold rate increase (τ_{SF} = 140 ps) and near fully efficient singlet fission with virtually no sacrifice in triplet lifetime. We thus illustrate novel design principles to produce favorable singlet fission properties, wherein through-space control can be achieved via coordination chemistry-induced multi-pentacene assembly.

Singlet fission is the organic analogue to multiple exciton generation (MEG), wherein single photon absorption by a chromophore yields one excited singlet state (S_1) that may relax into a correlated triplet pair $^{M}(T_1T_1)$ and, through decoherence, generate two free triplet states across multiple chromophores.[1,2] Although first discovered in polyacene crystals in the 1960's, singlet fission has received renewed attention over the past 15 years following the suggestion that MEG processes could be employed in photovoltaic devices to overcome the ~30% Shockley-Queisser limit of efficiency in single-junction solar cells.[3–11] Furthermore, the coherent properties of correlated triplet pairs suggest possible utilities of singlet fission materials in quantum information science and spintronic applications.[12–19]

If novel technologies with tailored singlet fission materials are to be realized, however, the structural and electronic origins of singlet fission require further elucidation.[2,20,21] Recently, covalently linked chromophores have arisen as an important tool to study intramolecular singlet fission, providing significant insight into the photophysics of this process.[20,22] In particular, molecular bipentacenes have received great attention owing to the exergonic and efficient nature of singlet fission in pentacene systems.[23,24] Systematic perturbations of the linkers as well as the position of chemical modification on the pentacene have revealed distinct fission rates and triplet pair or triplet state lifetimes.[20,25–38] In addition, recent investigations examined the effect of

through-space π-interactions on singlet fission and suggest the importance of slip-stacking geometric arrangements and Davydov splitting in the molecular excited states.[39,40] While the synthetic approach of systematic variation of a covalent linker has proven very versatile toward addressing a variety of fundamental aspects of singlet fission (Fig. 1), disentangling and controlling the through-bond and through-space effects that ultimately give rise to characteristic photophysical properties remains a challenge.

Herein we demonstrate how a single molecular bipentacene scaffold may give rise to tunable singlet fission properties by means of coordination-induced structural perturbations (Fig. 1). We have synthesized and studied the photophysics of a bipentacene displaying a dipyridyl pyrrolide motif capable of serving as a ligand for metal ions, with the lithium and potassium complexes reported here (Fig. 2). This series of complexes demonstrates the importance of

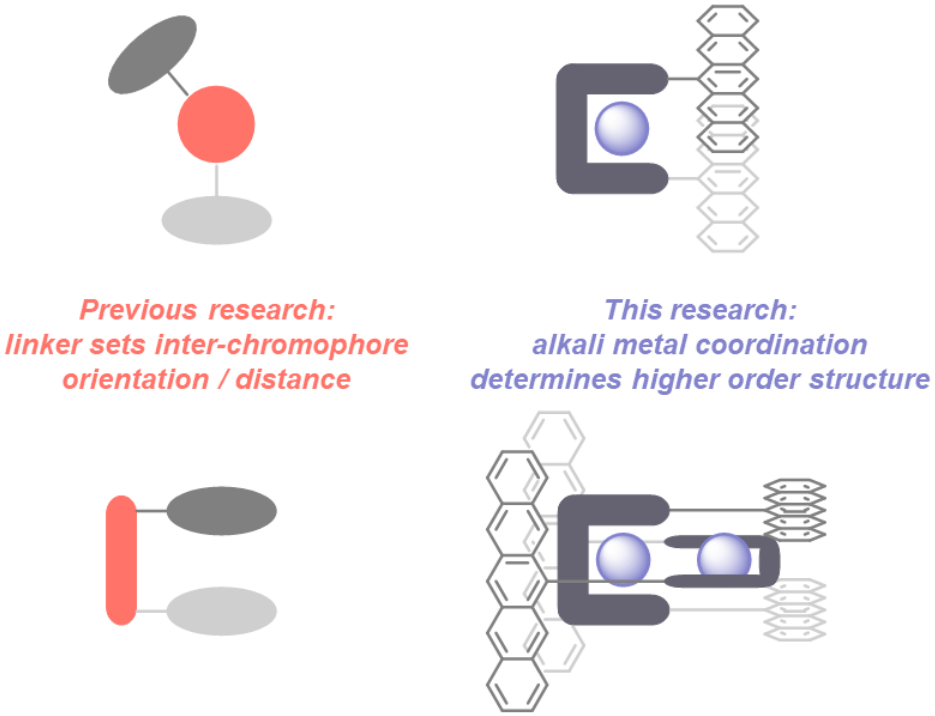

Figure 1. Coordination chemistry as a tool to organize bipentacene structure. Conceptual representations of previous approaches to bipentacene (and other bis-chromophore) structures and the present design for structural control promoted by metal binding.

designing and controlling the assembly of higher order structures for improved singlet fission performance. While maintaining the same covalent linker between chromophores, these compounds provide new design principles for the control of singlet fission via dimer self-assembly promoted by metal binding (Fig. 1).

Results & Analysis

Synthesis and NMR Characterization

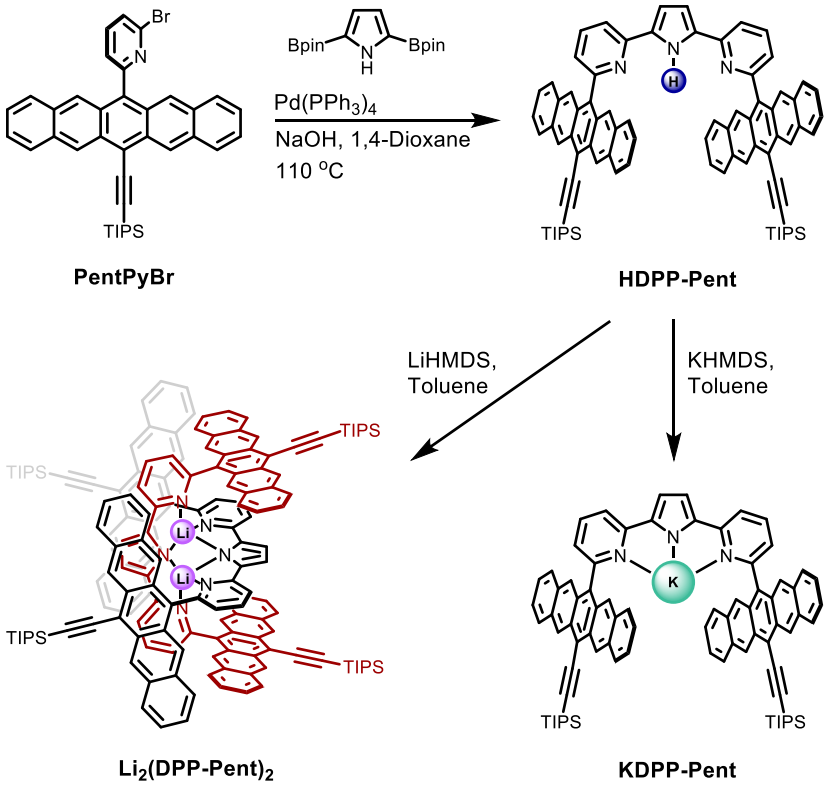

Figure 2. Synthesis of HDPP-Pent and MDPP-Pent Complexes.

The synthesis of the bipentacene, HDPP-Pent, displaying a dipyridyl pyrrole linker was performed from a monopentacene pyridyl bromide derivative (PentPyBr, Fig. 2). The ^{1}H NMR spectrum of HDPP-Pent (Supplementary Fig. S36) is relatively broad, particularly in the 6.5 – 9 ppm region, in contrast to the well-resolved scalar coupling between protons on the terminal rings

of the pentacene unit observed in the ^{1}H NMR spectrum of PentPyBr (Supplementary Fig. S34). While cooling from 20 to -80 °C, the variable temperature ^{1}H NMR data of HDPP-Pent display complex behavior. The aromatic region broadens considerably at -40 °C and subsequently a multitude of resonances grow in as the temperature is further decreased (Supplementary Fig. S38).

Deprotonation of HDPP-Pent with either lithium or potassium hexamethyldisilazide, leads to the formation of the lithium (Li_2(DPP-Pent)$_2$) or potassium (KDPP-Pent) complexes, respectively. In contrast to the broad NMR features observed in HDPP-Pent, deprotonation leads to sharp and well-defined ^{1}H NMR spectra for the alkali metal complexes at room temperature (Supplementary Figs. S39 and S40).

Upon closer comparison of the ^{1}H NMR spectra of the metal complexes, it is evident that the protons on the dipyridyl pyrrolide backbone of Li_2(DPP-Pent)$_2$ are significantly upfield shifted, unlike KDPP-Pent. For instance, the singlet corresponding to the pyrrolide ring proton is found at 4.38 ppm and 7.03 ppm in the Li_2(DPP-Pent)$_2$ and KDPP-Pent spectra, respectively. 2D rotating frame Overhauser enhancement spectroscopy (ROESY) experiments on Li_2(DPP-Pent)$_2$ also reveal through-space ^{1}H-^{1}H correlation between protons on the dipyridyl pyrrolide backbone at 4.38 ppm (H_c) and 5.14 ppm (H_d) and the proton on the distal side of the pentacene ring at 9.12 ppm (H_a) (denoted by green and blue circles, respectively, in Fig. 3b). Notably, no such cross peaks are observed in the 2D ROESY spectrum of KDPP-Pent (Fig. 3c).

Structural Analysis

The broadness of the room temperature ^{1}H NMR spectrum of HDPP-Pent along with the variable temperature behavior are indicative of solution-state conformational dynamics on the NMR timescale. These may involve rotations around aryl-aryl linkages that result in mixtures of conformers. The aromatic NMR features are resolved upon deprotonation and metal coordination

of the ligand framework, as evidenced by the sharp spectra observed for Li_2(DPP-Pent)$_2$ and KDPP-Pent, suggesting the formation of single conformers or fast exchange processes.

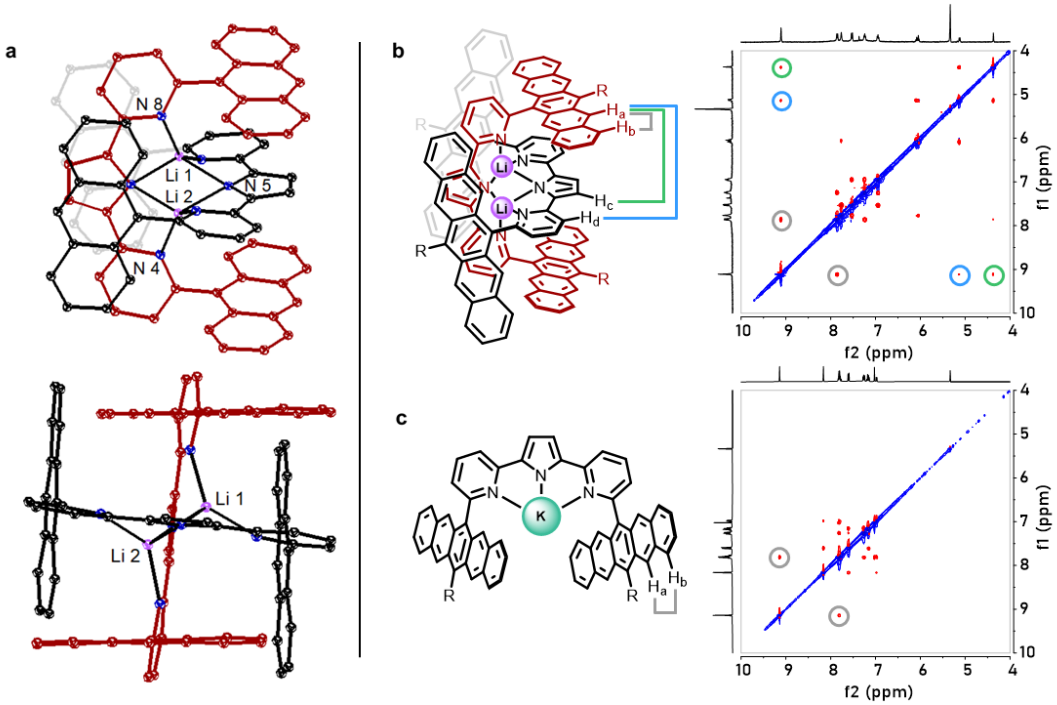

Figure 3. Structural data supporting dimeric Li_2(DPP-Pent)$_2$ and monomeric KDPP-Pent assignments in solution. (a) Crystallographic identification of a dimeric Li complex with an analogous ligand, DPP-Anth, in two perspectives. **(b)** The proposed dimeric structure of Li_2(DPP-Pent)$_2$ and the corresponding through-space coupling highlighted in the respective 2D-ROESY spectrum, and **(c)** the proposed monomeric structure of KDPP-Pent and the corresponding through-space coupling highlighted in the respective 2D-ROESY spectrum; R = triisopropylsilylethynyl.

The NMR data of Li_2(DPP-Pent)$_2$ strongly suggest a dimeric solution-state structure as proposed in Fig. 3b. The π-stacking interactions between the pentacene and sandwiched dipyridyl pyrrole units are consistent with the upfield shift exhibited by the dipyridyl pyrrole protons owing to enhanced chemical shielding by perturbation of the aromatic ring currents.[41,42] Likewise, the cross peaks in the 2D-ROESY spectrum between the pyrrole backbone protons and the protons on the far side of the pentacene support a dimeric structure. The dipolar couplings that give rise to the ROE are sensitive generally out to 5 Å, and a dimer would bring the relevant nuclei into proximity for this interaction.[43,44] Although X-ray quality single crystals of the pentacene derivatives have

eluded us, we have been able to crystallographically characterize a related lithium dipyridyl pyrrolide compound with anthracenyl instead of pentacenyl substituents, Li_2(DPP-Anth)$_2$ (Fig. 3a). This compound demonstrates the formation of a dimeric species with two lithium cations bridged by pyrrolide donors. As such, we propose Li_2(DPP-Pent)$_2$ has a similar geometry.

The NMR data for Li_2(DPP-Pent)$_2$ are in stark contrast to the NMR spectra of KDPP-Pent where the dipyridyl pyrrole backbone protons do not display either a significant upfield shift or observable cross peaks between pyrrole and distal pentacene protons in the ROESY spectrum. As such, we conclude that Li_2(DPP-Pent)$_2$ and KDPP-Pent have dimeric and monomeric solution state structures, respectively. The small ionic radius of Li^+ likely permits dimer formation, whereas the larger size of K^+ destabilizes such an interaction, enforcing a monomeric structure.

Steady-state Absorption and Emission

The steady-state absorption spectra of PentPyBr, HDPP-Pent, Li_2(DPP-Pent)$_2$, and KDPP-Pent are compared in Fig. 4a. The absorption spectrum of HDPP-Pent exhibits roughly twice the intensity of PentPyBr with little difference in peak positions within the vibronic progression of the $S_1 \leftarrow S_0$ absorption bands. The $S_1 \leftarrow S_0$ absorption in Li_2(DPP-Pent)$_2$ is slightly broadened, and the 0-0 band is modestly redshifted by 5 nm (~130 cm^{-1}) from that of HDPP-Pent. Additionally, both Li_2(DPP-Pent)$_2$ and KDPP-Pent exhibit enhanced absorption near 400-450 nm.

Steady-state emission spectra for PentPyBr and HDPP-Pent are compared in Fig. 4b. Here the 0-0 emission band of HDPP-Pent (λ_{max} = 650 nm, ~15,400 cm^{-1}) is red-shifted from the 0-0 band of PentPyBr (λ_{max} = 640 nm, ~15,600 cm^{-1}). The emission in this region is consistent with the $S_1 \rightarrow S_0$ fluorescence observed in similar pentacene compounds.[45] The fluorescence quantum yield of PentPyBr in toluene was determined to be 0.75, comparable to that reported for TIPS-Pentacene. The fluorescence quantum yield of HDPP-Pent, however, was found to be 0.43, significantly decreased relative to the single pentacene in PentPyBr. While $Li_2(DPP\text{-}Pent)_2$ and KDPP-Pent display similar emission profiles to HDPP-Pent, the integrated emission intensity is significantly reduced relative to HDPP-Pent.

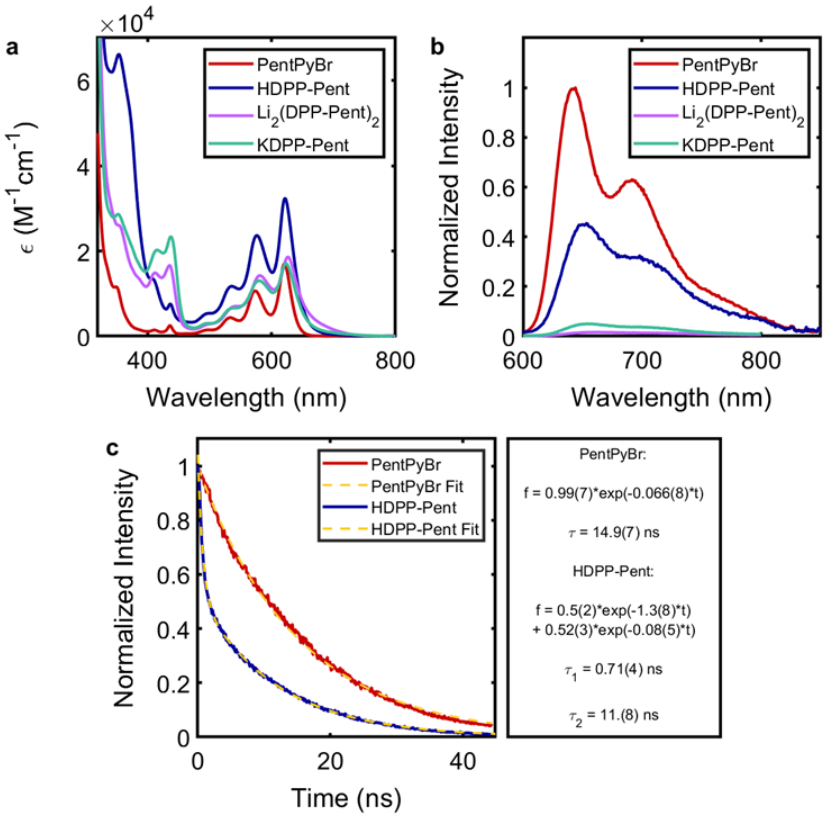

Figure 4. Steady-state absorption and emission spectra and time resolved-luminescence data of the pentacene series. Shown are the **(a)** absorption spectra **(b)** the normalized emission spectra of PentPyBr (red), HDPP-Pent (blue), $Li_2(DPP\text{-}Pent)_2$ (purple), and KDPP-Pent (green) in toluene solutions, and **(c)** time resolved luminescence traces and fits for PentPyBr (20 µM, toluene) and HDPP-Pent (20 µM, toluene). Note the steady-state emission spectra are normalized by their relative emission intensities.

Time-resolved luminescence

Time-resolved luminescence traces collected at 640 nm and 650 nm for PentPyBr and HDPP-Pent, respectively, are presented in Fig. 4c. The fluorescence decay for PentPyBr fits well to a monoexponential with a lifetime of ~15 ns. The fluorescence decay for HDPP-Pent, however, decays biexponentially with a first time constant of 0.71(4) ns and a second of 11.(8) ns, the latter of which is more consistent with the intrinsic fluorescence decay of the pentacene unit.

Emission Analysis

For efficient singlet fission (i.e. triplet yields approaching 200%), we expect the prompt fluorescence intensity to vanish, as the fission pathway must deplete the excited S_1 state more efficiently than emission. When singlet fission is sufficiently exothermic, which is the case for pentacene, the reverse triplet-triplet upconversion (fusion) becomes unfavorable, excluding delayed fluorescence. The observation of steady-state fluorescence intensity in HDPP-Pent already indicates that if singlet fission is occurring in this system, it is not operating at full efficiency. Nevertheless, the reduced fluorescence quantum yield for HDPP-Pent relative to PentPyBr suggests a new, non-emissive relaxation pathway is present in the bipentacene that is not observed in the monopentacene.

This is borne out by comparing the time-resolved luminescence spectra of PentPyBr and HDPP-Pent. The monoexponential decay of the fluorescence signal in PentPyBr is consistent with that expected for an emissive process. The time-resolved signal in HDPP-Pent must be fit with at least a biexponential function with time constants τ_1 = 0.71(4) ns and τ_2 = 11.(8) ns and weighting coefficients of roughly 0.5 each. The latter time constant is closer to the decay observed in PentPyBr and may be associated with the intrinsic emissive relaxation within HDPP-Pent. The

0.71(4) ns exponential time constant therefore likely corresponds to the competitive non-emissive relaxation pathway.

Transient Absorption Spectroscopy – HDPP-Pent

To provide deeper insight into the nature of the competitive nonradiative relaxation process in HDPP-Pent, we performed femtosecond transient absorption (fsTA) spectroscopy on PentPyBr and HDPP-Pent. The fsTA data of PentPyBr (Supplementary Fig. S13) reveal a single major excited state absorption (ESA) centered at 450 nm (~22,200 cm^{-1}), which has previously been assigned to absorption within the singlet excited state manifold (^{1}ESA) of related pentacene

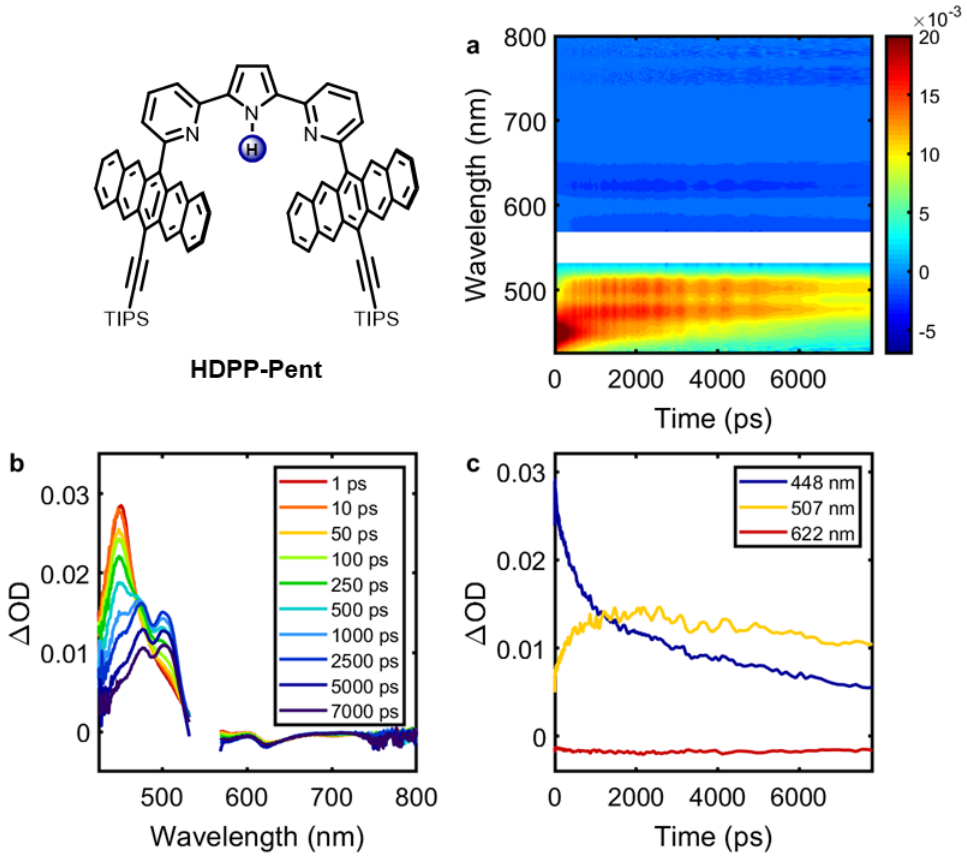

Figure 5. Visible transient absorption spectra – HDPP-Pent. The visible femtosecond transient absorption spectra of HDPP-Pent (50 µM, toluene) after excitation at 550 nm (0.100 µJ/pulse) are depicted: (a) contour plot, (b) spectral traces at various time delays, (c) selected time traces at 448, 507, and 622 nm.

compounds.[25,26,45] This ^{1}ESA decays monoexponentially over the time window, consistent with the time-resolved fluorescence data.

The fsTA data for HDPP-Pent are given in Fig. 5. A ^{1}ESA at 450 nm is observed at early time delays, but it decays across the fsTA spectrum with the concomitant rise of a new, structured absorption feature at λ_{max} = 507 nm (~19,700 cm^{-1}). This new feature is consistent with previous literature reports that assign this band to transitions arising from either the triplet pair or free triplet state (^{3}ESA).[25,26,45] This ^{3}ESA is not appreciably observed for PentPyBr. The nanosecond TA (nsTA) data for HDPP-Pent (Supplementary Fig. S9) reveal the full decay of the ^{3}ESA feature. The comparison between PentPyBr and HDPP-Pent TA data suggests the nonradiative pathway in HDPP-Pent may be associated with a transition from the S_1 to the T_1 or ^{M}(TT) states, as indicated by the rise of the prominent ^{3}ESA feature.

Kinetic Modelling

Kinetic modelling was carried out via target analysis on a composite dataset of the fsTA and nsTA spectra of HDPP-Pent in order to capture the complete dynamics. Using target analysis, the entire TA dataset is fit over all wavelengths and all time delays with the application of a kinetic model. The preparation of the composite dataset and a full description of the model applied to HDPP-Pent is provided in Supplementary Information Section VII along with fits for the individual fsTA and nsTA spectra for reference.

The time-resolved luminescence data were applied as an independent probe of the S_1 dynamics, leading to a four component model in which components 1 and 2 equally reflect the ^{1}ESA spectrum and components 3 and 4 represent the ^{3}ESA spectrum. Component 1 decays into components 3 and 4 equally with a rate constant k_1, component 2 decays to the ground state with

rate constant k_2, and components 3 and 4 decay to the ground state decay with rate constants k_3 and k_4, respectively.

This model was applied in two cases: one in which k_1 and k_2 were allowed to vary freely, and one in which k_1 and k_2 were fixed to 1.4 ns^{-1} and 0.08 ns^{-1}, respectively, as obtained directly from the time-resolved fluorescence fits. The results of the free and fixed fittings are shown in Supplementary Tables S1 and S2, respectively. Of note, the results for k_1, k_3, and k_4 are remarkably consistent between the two fits. Even when allowed to vary, the fit of k_1 gives a time constant τ_1 of 0.74(6) ns, consistent with the τ ~0.71 ns obtained from the emission data. This k_1 corresponds to the nonradiative transition from S_1 to T_1 within our model. k_2 shows the largest divergence in the two fits: τ_2 = 4.9(5) ns when allowed to vary from the fixed value of 11.(8) ns. Both values are consistent with the radiative lifetime, though the error may come from the convolution of spectral features in the combined fs/nsTA data.

Triplet Yield Estimation –HDPP-Pent

The triplet yield after direct excitation of HDPP-Pent was estimated from the TA data and the target kinetic modelling. First, the extinction coefficient of the ^{3}ESA at 510 nm was determined by the triplet energy transfer method using a donor of known triplet molar absorptivity (anthracene) under pseudo-first order kinetic conditions (Supplementary Information, Section VIII).[46–48] From this, we approximate the ^{3}ESA molar absorptivity of HDPP-Pent at 510 nm to be 49,000 M^{-1} cm^{-1} (Supplementary Fig. S33).[45,26]

As is shown explicitly in Section IX of the Supplementary Information, the target model can be used to decompose the maximum ΔOD into its contributions from the ^{1}ESA and ^{3}ESA as 2.8 and 10.0 mOD respectively. Thus, after direct excitation of HDPP-Pent in toluene solution, the value of 10.0 mOD for the effective ^{3}ESA intensity provides an estimated triplet yield of ~100%.

Analysis of Singlet Fission in HDPP-Pent

Comparison between steady-state and time-resolved emission data for HDPP-Pent and PentPyBr indicates a distinct nonradiative relaxation pathway is present in the bipentacene HDPP-Pent that is not significant in the monopentacene reference. To interrogate this pathway further, we examined the fs/nsTA data for both samples. In HDPP-Pent, the decay of the ^{1}ESA gave rise to significant ^{3}ESA intensity, whereas in PentPyBr, only the decay of the ^{1}ESA was observed. The HDPP-Pent data were modelled given a kinetic scheme in which the S_1 decays in two pathways and supports the assignment of the non-emissive relaxation observed in the time-resolved luminescence to be associated with singlet to triplet conversion.

Finally, the triplet yield of HDPP-Pent is estimated to be 100% out of a maximum of 200%. As previously noted, the fluorescence quantum yield of HDPP-Pent is 43%. The weighting coefficients of the exponential decays observed in the time-resolved luminescence data are also ~0.5 each. Taken together, these data are self-consistent with a model in which nearly half of the photogenerated singlets give rise to twice the number of triplets. The nonradiative transition in HDPP-Pent may thus be assigned as intramolecular singlet fission.

Li_2(DPP-Pent)$_2$ and KDPP-Pent

The HDPP-Pent analysis provides a foundation to understand the dynamics exhibited by the alkali metal complexes. The fsTA data for Li_2(DPP-Pent)$_2$ is shown in Fig. 6a-c. At early time delays, there is a ^{1}ESA feature at λ_{max} = 450 nm that decays and gives rise to a strong ^{3}ESA centered at 515 nm (~19,400 cm^{-1}). The composite fs/nsTA data can be kinetically modelled well with just three components (Supplementary Table S5), in which the S_1 state is fully converted to the triplet manifold with a time constant τ_1 of ~140 ps; the triplet feature is then fit to a biexponential decay

with time constants τ_2 and τ_3 of 25.1(1) ns and 42.(0) µs, respectively. Along with the lack of steady-state fluorescence intensity, these data strongly suggest a highly efficient singlet fission pathway in Li_2(DPP-Pent)$_2$, approaching 200% triplet yield.

In the case of KDPP-Pent, the fsTA data show the decay of the ^{1}ESA to a broad feature suggestive of the overlapping singlet and triplet absorption bands observed in HDPP-Pent (Fig. 6d-f). The nsTA data reveal a structured ^{3}ESA that decays biexponentially in the KDPP-Pent sample. The kinetics could be fit with both the three-component model applied to the Li_2(DPP-Pent)$_2$ dataset and a four-component model used for HDPP-Pent (Supplementary Tables S8 and S9). There is some absorption intensity in the 400 – 500 nm region in the singular value decomposition of the residual data matrix of the three-component fit that is adequately accounted for in the four-component model. With regards to the two models, the fittings place a singlet fission

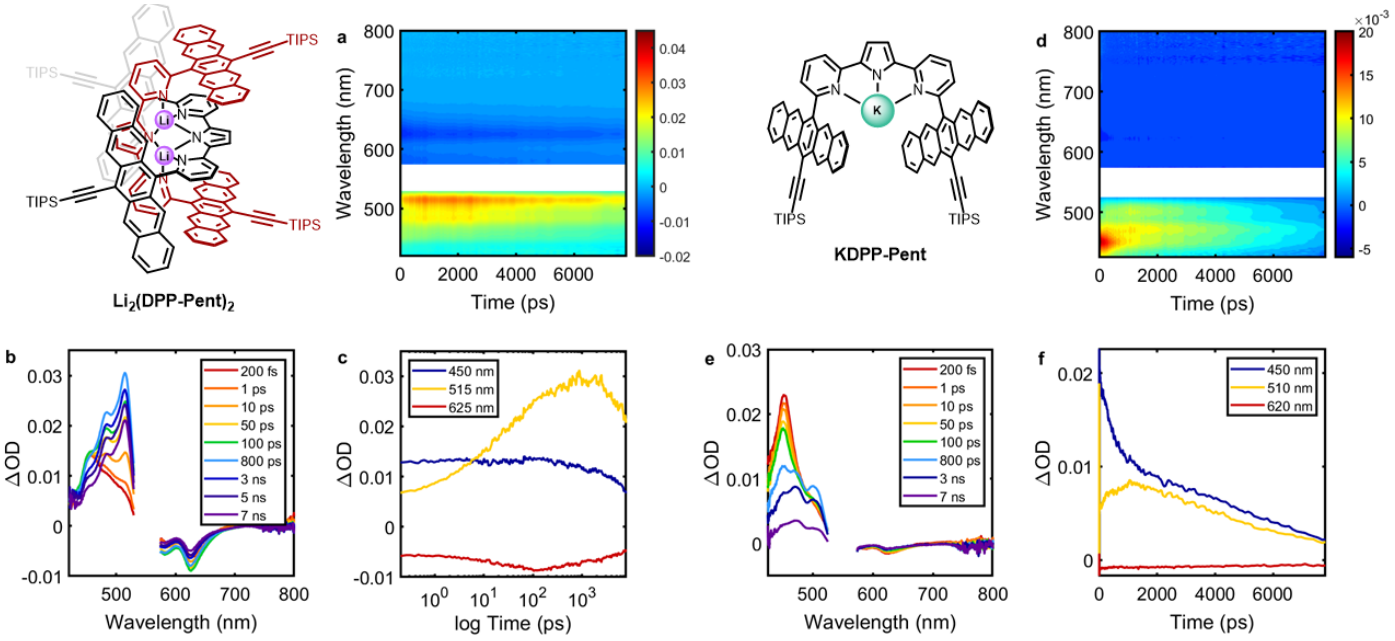

Figure 6. Visible transient absorption spectra – Li_2(DPP-Pent)$_2$ and KDPP-pent. The visible femtosecond transient absorption spectra of Li_2(DPP-Pent)$_2$ and KDPP-Pent (50 µM, toluene) are shown after excitation at 550 nm (0.100 µJ/pulse); Li_2(DPP-Pent)$_2$: (a) contour plot, (b) spectral traces at various time delays, (c) selected time traces at 450, 515, and 625 nm, KDPP-Pent: (d) contour plot, (e) spectral traces at various delay times, (f) selected time traces at 450, 510, and 620 nm.

time constant in KDPP-Pent around 400 – 600 ps. Despite the qualitative similarity between the K- and HDPP-Pent TA data, little emission intensity was observed from the K complex and no time-resolved luminescence could be acquired, which suggests that KDPP-Pent may represent an intermediate case between HDPP-Pent and the Li complex.

Discussion

HDPP-Pent undergoes intramolecular singlet fission with a time constant τ_{SF} of ~730 ps with an estimated 100% triplet yield. In contrast, singlet fission in Li_2(DPP-Pent)$_2$ (τ_{SF} ~140 ps) is nearly five-fold faster than HDPP-Pent and occurs with nearly full efficiency (i.e., 200% triplet yield). KDPP-Pent, on the other hand, demonstrates a rate of fission (τ_{SF} ~400-600 ps) more akin to HDPP-Pent.

There are several considerations for the origin of the rate enhancement in Li_2(DPP-Pent)$_2$. First, the NMR data demonstrate temperature dependent conformational dynamics in HDPP-Pent, which suggests a heterogeneity of conformations are excited in solution during the TA experiment, some of which may be less favorable for intramolecular singlet fission than others. Deprotonation and complexation may rigidify the linker, leading to more efficient singlet fission in solution. However, the Li and K complexes both display well-resolved ^{1}H NMR spectra, unlike the spectrum of HDPP-Pent, and therefore the structural rigidification alone does not explain the rate enhancement in Li_2(DPP-Pent)$_2$.

Second, the ionic pyrrolide-cation interaction introduces an electric dipole in the vicinity of the pentacene subunits, where a potential Stark effect could influence singlet fission within the system. The Li and K complexes would likely exhibit distinct electric field influences, but at this point it is unclear the extent to which this would differentiate the two.

Third, NMR data support the assignment of dimeric and monomeric solution-state structures for Li_2(DPP-Pent)$_2$ and KDPP-Pent, respectively. The Li complex is thus distinct from the K structure, as it exhibits π-stacking interactions between pentacene subunits through a middle dipyridyl pyrrolide moiety and also has four pentacene rings in a single molecular unit as opposed to two (Figure 3). It is likely that these structural perturbations lead to a pronounced rate enhancement in Li_2(DPP-Pent)$_2$ relative to KDPP-Pent. The interactions established via π-stacking may promote favorable electronic coupling, leading to efficient fission. The increased number of pentacene units in the dimer may also favor a faster rate of singlet fission. For example, by comparing adamantyl-linked bi- and tetra-pentacene systems, Hetzer et al. suggested additional chromophores may effectively delocalize the triplet pair state, providing a favorable entropic factor to the rate of fission.[35]

Notably, despite the five-fold rate enhancement in Li_2(DPP-Pent)$_2$, there is little sacrifice in terms of triplet lifetimes – all species in the series studied here demonstrate biexponential triplet lifetimes with short- and long-lived time components in the 25 – 40 ns and 35 – 45 μs ranges, respectively. The fast time component of the triplet decay has been proposed to be a result of geminate recombination from the triplet pair state, whereas the long time component is consistent with a sensitized triplet lifetime.[22] Amongst other literature examples, however, there is typically an increase in the rate of triplet decay when stronger coupling between pentacene units results in faster rates of fission (Supplementary Table S13).[22] The structural control over the two chromophores demonstrated here is thus significant with respect to achieving efficient singlet fission without concomitant acceleration of triplet pair decay pathways.

In summary, with HDPP-Pent and its alkali metal derivatives, we have demonstrated the ability to tune singlet fission via supramolecular assembly promoted by metal coordination. The

π-stacking interactions and dimeric structure revealed in $Li_2(DPP\text{-}Pent)_2$ are critical to its increased singlet fission efficiency compared to the parent HDPP-Pent. This approach highlights the importance of through-space, geometric perturbations that influence singlet fission beyond strict through-bond interactions. Controlling the orientation and interaction of multiple pentacene motifs through coordination chemistry is demonstrated as a new, impactful tool for improving singlet fission performance.

Methods

Steady-state Emission Spectroscopy

Corrected room temperature emission spectra were collected in the Beckman Institute Laser Resource Center using a modified Jobin Yvon Spec Fluorolog-3 instrument. Samples were excited with a xenon arc lamp, employing a monochromator for wavelength selection, and emission was detected at 90° using two Ocean Optics EQDPro CCD spectrometers spanning 300 to 930 nm.

Fluorescence quantum yields were determined via the comparative method in which the experimental quantum yields were measured relative to a known standard under the same excitation conditions. Rhodamine-6G in EtOH was used as a standard ($\Phi_S = 0.95$). All samples were diluted such that the maximum absorbance values were less than 0.1. Pentacene samples of unknown quantum yield were prepared in toluene and added to 1 cm glass emission cuvettes and sealed with a Kontes plug under $N_{2(g)}$ atmosphere. Samples were excited at $\lambda_{ex} = 530$ nm. The unknown quantum yields (Φ_X) were calculated with Equation 1 using the absorbance values $A(\lambda_{ex})$, the integrated fluorescence intensities $F(\lambda_{ex})$, and correcting for the differing indices of refraction between EtOH and toluene.

$$\Phi_X = \frac{A_S(\lambda_{ex})}{A_X(\lambda_{ex})} \cdot \frac{F_X(\lambda_{ex})}{F_S(\lambda_{ex})} \cdot \frac{n_X^2}{n_S^2} \cdot \Phi_S \qquad Eq\ (1)$$

Time-resolved Luminescence Spectroscopy

The 1064 nm output of a Nd:YAG laser (Spectra Physics Vanguard) was regeneratively amplified (Continuum) and frequency doubled using a potassium dihydrogen phosphate (KDP) crystal to 532 nm excitation pulses (~10 ps, 10 Hz). Luminescence was collected 90° from the excitation, passed through a polarizer oriented at the magic angle, then directed onto the entrance slit of a monochromator for wavelength selection. Detection was achieved using a streak camera (Hamamatsu C5680) in photon-counting mode and data were collected over a 50 ns time window. Samples were prepared in sealed 1 cm quartz cuvettes under $N_{2(g)}$ and were stirred during data acquisition.

Transient Absorption Spectroscopy

The 800 nm output of a 5 W, 1 kHz pulsed Ti:sapphire amplifier (Coherent Astrella) was partitioned with a 50:50 beamsplitter. One half was fed into an OPerA Solo optical parametric amplifier tuned to 550 nm output, which was used as the excitation pump and routed through a chopper and into a joint femtosecond and nanosecond HELIOS FIRE / EOS transient absorption (TA) spectrometer (Ultrafast Systems). For femtosecond experiments, a small portion of the other half of the Ti:sapphire output was routed into the spectrometer and used to generate broadband probe light of the appropriate wavelength region (visible or near-infrared). For nanosecond experiments, a separate white light fiber laser was employed as the probe light. Samples were prepared in sealed 2 mm glass cuvettes under $N_{2(g)}$ and were stirred during data acquisition. Data were processed using Ultrafast Systems Surface Xplorer software for chirp and time zero corrections. The rest of the data workup was performed in MATLAB. For fsTA datasets, pre-time

zero spectral vectors were averaged and subtracted from the rest of the dataset to remove background pump scatter. Pre-time zero spectral vectors were similarly averaged in the nsTA datasets and then subtracted up to 20 μs delay times as pump scatter is not detected beyond this threshold by the EOS.

Acknowledgments. The authors thank Dr. Jay Winkler for assistance with time-resolved luminescence measurements, the Beckman Institute Laser Resource Center (BILRC) for access to the associated equipment, and Dr. David VanderVelde for NMR support and helpful discussions. Mike Takase and Larry Henling are acknowledged for crystallographic assistance. TA is grateful for the support provided by King Fahd University of Petroleum and Minerals, Dhahran, Saudi Arabia, offered under the KFUPM-Caltech Research Collaboration and the Joint Center for Artificial Photosynthesis, a DOE Energy Innovation Hub, supported through the Office of Science of the U.S. Department of Energy under Award Number DE-SC0004993. Financial support from Caltech and the Dow Next Generation Educator Fund is gratefully acknowledged (RGH).

References

1. Smith, M. B. & Michl, J. Singlet Fission. *Chem. Rev.* **110**, 6891–6936 (2010).
2. Smith, M. B. & Michl, J. Recent Advances in Singlet Fission. *Annual Review of Physical Chemistry* **64**, 361–386 (2013).
3. Swenberg, C. E. & Stacy, W. T. Bimolecular radiationless transitions in crystalline tetracene. *Chemical Physics Letters* **2**, 327–328 (1968).
4. Merrifield, R. E., Avakian, P. & Groff, R. P. Fission of singlet excitons into pairs of triplet excitons in tetracene crystals. *Chemical Physics Letters* **3**, 155–157 (1969).
5. Merrifield, R. E. Magnetic effects on triplet exciton interactions. *Pure and Applied Chemistry* **27**, 481–498 (1971).
6. Shockley, W. & Queisser, H. J. Detailed Balance Limit of Efficiency of p-n Junction Solar Cells. *Journal of Applied Physics* **32**, 510–519 (1961).
7. Hanna, M. C. & Nozik, A. J. Solar conversion efficiency of photovoltaic and photoelectrolysis cells with carrier multiplication absorbers. *Journal of Applied Physics* **100**, 074510 (2006).
8. Paci, I. *et al.* Singlet Fission for Dye-Sensitized Solar Cells: Can a Suitable Sensitizer Be Found? *J. Am. Chem. Soc.* **128**, 16546–16553 (2006).
9. Rao, A. *et al.* Exciton Fission and Charge Generation via Triplet Excitons in Pentacene/C60 Bilayers. *J. Am. Chem. Soc.* **132**, 12698–12703 (2010).
10. Ehrler, B., Wilson, M. W. B., Rao, A., Friend, R. H. & Greenham, N. C. Singlet Exciton Fission-Sensitized Infrared Quantum Dot Solar Cells. *Nano Lett.* **12**, 1053–1057 (2012).
11. Ehrler, B., Musselman, K. P., Böhm, M. L., Friend, R. H. & Greenham, N. C. Hybrid pentacene/a-silicon solar cells utilizing multiple carrier generation via singlet exciton fission. *Appl. Phys. Lett.* **101**, 153507 (2012).

12. Weiss, L. R. *et al.* Strongly exchange-coupled triplet pairs in an organic semiconductor. *Nature Physics* **13**, 176–181 (2017).
13. Tayebjee, M. J. Y. *et al.* Quintet multiexciton dynamics in singlet fission. *Nature Physics* **13**, 182–188 (2017).
14. Bayliss, S. L. *et al.* Site-selective measurement of coupled spin pairs in an organic semiconductor. *PNAS* **115**, 5077–5082 (2018).
15. Lubert-Perquel, D. *et al.* Identifying triplet pathways in dilute pentacene films. *Nature Communications* **9**, 4222 (2018).
16. Wan, Y., Wiederrecht, G. P., Schaller, R. D., Johnson, J. C. & Huang, L. Transport of Spin-Entangled Triplet Excitons Generated by Singlet Fission. *J. Phys. Chem. Lett.* 6731–6738 (2018) doi:10.1021/acs.jpclett.8b02944.
17. Nagashima, H. *et al.* Singlet-Fission-Born Quintet State: Sublevel Selections and Trapping by Multiexciton Thermodynamics. *J. Phys. Chem. Lett.* **9**, 5855–5861 (2018).
18. Chen, M. *et al.* Quintet-triplet mixing determines the fate of the multiexciton state produced by singlet fission in a terrylenediimide dimer at room temperature. *PNAS* **116**, 8178–8183 (2019).
19. Matsuda, S., Oyama, S. & Kobori, Y. Electron spin polarization generated by transport of singlet and quintet multiexcitons to spin-correlated triplet pairs during singlet fissions. *Chem. Sci.* **11**, 2934–2942 (2020).
20. Hetzer, C., Guldi, D. M. & Tykwinski, R. R. Pentacene Dimers as a Critical Tool for the Investigation of Intramolecular Singlet Fission. *Chemistry – A European Journal* **24**, 8245–8257 (2018).

21. Sanders, S. N. *et al.* Understanding the Bound Triplet-Pair State in Singlet Fission. *Chem* **5**, 1988–2005 (2019).
22. Korovina, N. V., Pompetti, N. F. & Johnson, J. C. Lessons from intramolecular singlet fission with covalently bound chromophores. *J. Chem. Phys.* **152**, 040904 (2020).
23. Wilson, M. W. B. *et al.* Ultrafast Dynamics of Exciton Fission in Polycrystalline Pentacene. *J. Am. Chem. Soc.* **133**, 11830–11833 (2011).
24. Rao, A., Wilson, M. W. B., Albert-Seifried, S., Di Pietro, R. & Friend, R. H. Photophysics of pentacene thin films: The role of exciton fission and heating effects. *Phys. Rev. B* **84**, 195411 (2011).
25. Zirzlmeier, J. *et al.* Singlet fission in pentacene dimers. *PNAS* **112**, 5325–5330 (2015).
26. Sanders, S. N. *et al.* Quantitative Intramolecular Singlet Fission in Bipentacenes. *J. Am. Chem. Soc.* **137**, 8965–8972 (2015).
27. Zirzlmeier, J. *et al.* Solution-based intramolecular singlet fission in cross-conjugated pentacene dimers. *Nanoscale* **8**, 10113–10123 (2016).
28. Sanders, S. N. *et al.* Exciton Correlations in Intramolecular Singlet Fission. *J. Am. Chem. Soc.* **138**, 7289–7297 (2016).
29. Sanders, S. N. *et al.* Intramolecular Singlet Fission in Oligoacene Heterodimers. *Angewandte Chemie International Edition* **55**, 3373–3377 (2016).
30. Fuemmeler, E. G. *et al.* A Direct Mechanism of Ultrafast Intramolecular Singlet Fission in Pentacene Dimers. *ACS Cent. Sci.* **2**, 316–324 (2016).
31. Kumarasamy, E. *et al.* Tuning Singlet Fission in π-Bridge-π Chromophores. *J. Am. Chem. Soc.* **139**, 12488–12494 (2017).

32. Basel, B. S. *et al.* Evidence for Charge-Transfer Mediation in the Primary Events of Singlet Fission in a Weakly Coupled Pentacene Dimer. *Chem* **4**, 1092–1111 (2018).
33. Mandal, A. *et al.* Two-Dimensional Electronic Spectroscopy Reveals Excitation Energy-Dependent State Mixing during Singlet Fission in a Terrylenediimide Dimer. *J. Am. Chem. Soc.* **140**, 17907–17914 (2018).
34. Papadopoulos, I. *et al.* Varying the Interpentacene Electronic Coupling to Tune Singlet Fission. *J. Am. Chem. Soc.* **141**, 6191–6203 (2019).
35. Hetzer, C. *et al.* Chromophore Multiplication To Enable Exciton Delocalization and Triplet Diffusion Following Singlet Fission in Tetrameric Pentacene. *Angewandte Chemie International Edition* **58**, 15263–15267 (2019).
36. Casillas, R. *et al.* Intermolecular Singlet Fission in Unsymmetrical Derivatives of Pentacene in Solution. *Advanced Energy Materials* **9**, 1802221 (2019).
37. S. Basel, B. *et al.* Influence of the heavy-atom effect on singlet fission: a study of platinum-bridged pentacene dimers. *Chemical Science* **10**, 11130–11140 (2019).
38. Papadopoulos, I., Gao, Y., Hetzer, C., Tykwinski, R. R. & Guldi, D. M. Singlet Fission in Enantiomerically Pure Pentacene Dimers. *ChemPhotoChem* **n/a**, (2020).
39. Sabine Basel, B. *et al.* Davydov splitting and singlet fission in excitonically coupled pentacene dimers. *Chemical Science* **10**, 3854–3863 (2019).
40. Chen, M. *et al.* Singlet Fission in Covalent Terrylenediimide Dimers: Probing the Nature of the Multiexciton State Using Femtosecond Mid-Infrared Spectroscopy. *J. Am. Chem. Soc.* **140**, 9184–9192 (2018).

41. Shetty, A. S., Zhang, J. & Moore, J. S. Aromatic π-Stacking in Solution as Revealed through the Aggregation of Phenylacetylene Macrocycles. *J. Am. Chem. Soc.* **118**, 1019–1027 (1996).
42. A. Platts, J. & Gkionis, K. NMR shielding as a probe of intermolecular interactions: ab initio and density functional theory studies. *Physical Chemistry Chemical Physics* **11**, 10331–10339 (2009).
43. Bothner-By, A. A., Stephens, R. L., Lee, J., Warren, C. D. & Jeanloz, R. W. Structure determination of a tetrasaccharide: transient nuclear Overhauser effects in the rotating frame. *J. Am. Chem. Soc.* **106**, 811–813 (1984).
44. Bax, A. & Davis, D. G. Practical aspects of two-dimensional transverse NOE spectroscopy. *Journal of Magnetic Resonance (1969)* **63**, 207–213 (1985).
45. Walker, B. J., Musser, A. J., Beljonne, D. & Friend, R. H. Singlet exciton fission in solution. *Nature Chemistry* **5**, 1019–1024 (2013).
46. Bensasson, R. & Land, E. J. Triplet-triplet extinction coefficients via energy transfer. *Trans. Faraday Soc.* **67**, 1904–1915 (1971).
47. Compton, R. H., Grattan, K. T. V. & Morrow, T. Extinction coefficients and quantum yields for triplet—triplet absorption using laser flash photolysis. *Journal of Photochemistry* **14**, 61–66 (1980).
48. Nielsen, B. R., Jørgensen, K. & Skibsted, L. H. Triplet—triplet extinction coefficients, rate constants of triplet decay and rate constant of anthracene triplet sensitization by laser flash photolysis of astaxanthin, β-carotene, canthaxanthin and zeaxanthin in deaerated toluene at 298 K. *Journal of Photochemistry and Photobiology A: Chemistry* **112**, 127–133 (1998).

Supplementary Information

Controlling Singlet Fission with Coordination Chemistry-Induced Structural Perturbations in a Series of Dipyridyl Pyrrole Bipentacenes

Ryan D. Ribson[1], Gyeongshin Choi[1], Ryan G. Hadt[1]*, Theodor Agapie[1]*

[1]Division of Chemistry and Chemical Engineering, Arthur Amos Noyes Laboratory of Chemical Physics, California Institute of Technology, Pasadena, California 91125, United States

*Corresponding authors: rghadt@caltech.edu, agapie@caltech.edu

I. Experimental Considerations

General Information

Air- and moisture-sensitive compounds were handled with standard Schlenk line techniques or in a $N_{2(g)}$ atmosphere glove box. When air- and moisture-free techniques were required, dry solvents were acquired from an alumina solvent still. 2,6-dibromopyridine was purchased from Combi-Blocks Inc. and used without further purification. Tin (II) dichloride dihydrate was purchased from Matrix Scientific and used without further purification. $Pd(PPh_3)_4$ was purchased from Oakwood Chemicals, stored under inert atmosphere, and used without further purification. Lithium hexamethyldisilazide and potassium hexamethyl disilazide were purchased from Sigma Aldrich, stored in an inert atmosphere glovebox, and used without further purification. 13-hydroxy-13-[(triisopropylsilyl)ethynyl]pentacen-6(13H)-one (Ketone 1, Figure S1)[1] and 2,5-bis(pinacolatoboranyl)pyrrole[2] were synthesized according to previous reports. ^{1}H, ^{13}C, and 2D NMR spectra were collected on a 400 MHz Varian spectrometer. All pentacene solution-state samples for optical spectroscopy were prepared in an inert-atmosphere glovebox using solvents dried and purified on an alumina drying column and degassed prior to being brought into the glovebox. Steady state absorption spectra were collected using a Varian Cary 500 Scan spectrophotometer. Glotaran (http://glotaran.org), a user interface for the R-based time-resolved fitting software TIMP, was used for kinetic modelling of the transient absorption data.[3]

II. Synthetic Procedures

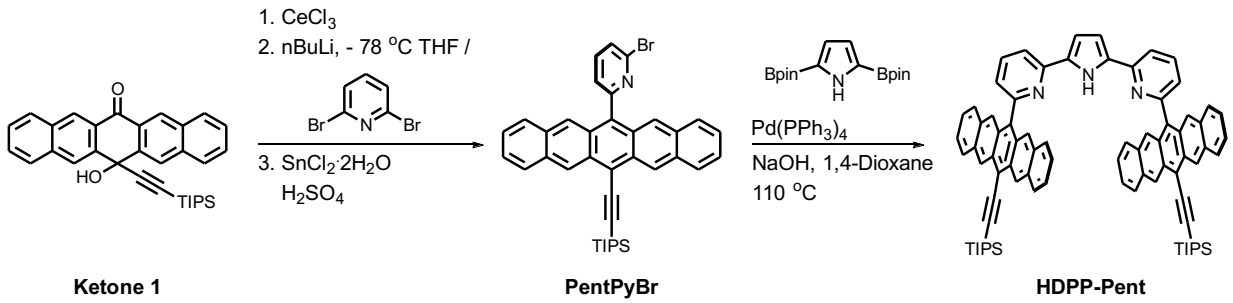

Figure S1. Synthetic scheme for HDPP-Pent. Ketone 1 is activated with $CeCl_3$ then converted into PentPyBr by deprotonation and nucleophilic attack by monolithiated 2,6-dibromopyridine at -78 °C, followed by reductive aromatization with $SnCl_2 \cdot 2H_2O$. HDPP-Pent is then furnished after a double-Suzuki-Miyaura coupling of PentPyBr with 2,5-bis(pinacolatoboranyl)pyrrole using catalytic $Pd(PPh_3)_4$.

Synthesis of PentPyBr

Ketone 1 (10 mmol) was dissolved in THF in an oven-dried flask under inert conditions. $CeCl_3$ (20 mmol) was added under positive $N_{2(g)}$ pressure and the mixture was stirred for 1 h at room temperature. In a separate flask under nitrogen atmosphere, dibromopyridine (30 mmol) was dissolved in THF and cooled to -78 °C. nBuLi (1.6M solution in hexanes, 30 mmol) was then added slowly to the pyridine solution, which was stirred for 30 min to achieve monolithiation. The solution of Ketone 1 was cooled to -78 °C and the lithiated pyridine solution was slowly cannula transferred under positive nitrogen pressure with stirring. The mixture was warmed to room temperature and stirred for 15 h. Aqueous ammonium chloride solution was slowly added to quench. The brown solution was filtered through a pad of celite to remove salts. The organics were taken up in dichloromethane and washed with brine (2x), dried over Mg_2SO_4, and concentrated to an oily solid. This material was taken up in THF (80 mL) and transferred to a three neck roundbottom flask. The solution was sparged with $N_{2(g)}$ and $SnCl_2 \cdot 2H_2O$ (20 mmol) was added followed by slow addition of 10% H_2SO_4 (3 mL). The solution was sparged again and stirred for 3 h under nitrogen atmosphere at room temperature. The reaction was neutralized with $K_2CO_{3(aq)}$ and the reaction mixture was filtered through celite. The product was extracted with dichloromethane and dried over Mg_2SO_4. The mixture was concentrated, and the target compound was crashed from methanol to give a dark blue powder. ^{1}H NMR (400 MHz, $CDCl_3$, 25 ºC): δ 9.37 (s, 2H), 8.16 (s, 2H), 7.96 (d, J = 8.5 Hz, 2H), 7.93 – 7.89 (m, 1H), 7.81 (dd, J = 8.0, 1.0 Hz, 1H), 7.77 (d, J = 8.5 Hz, 2H), 7.60 (dd, J = 7.4, 1.0 Hz, 1H), 7.40 – 7.29 (m, 5H), 1.39 (s, 21H). ^{13}C NMR (101 MHz, $CDCl_3$, 25 ºC): δ 159.7, 142.7, 139.0, 134.0, 132.0, 130.9, 128.8, 128.7, 128.3, 127.5, 126.5, 126.2, 126.1, 125.9, 125.1, 119.2, 106.4, 104.7, 19.2, 11.8. HRMS (FAB+) Calcd. For $C_{38}H_{36}NSiBr$: 615.1780. Found: 615.1770.

Synthesis of HDPP-Pent

PentPyBr (2.5 g), 2,5-bis(pinacolatoboranyl)pyrrole (0.65 mg), and NaOH (8.7 mg) were added to an oven-dried Schlenk flask under nitrogen atmosphere and a degassed 9:1 1,4-dioxane/H_2O solution (100 mL) was added. $Pd(PPh_3)_4$ (5 mol%) was added under a counter-flow of $N_{2(g)}$ and the reaction mixture was heated to 110 °C for 5 h. Volatiles were removed under vacuum pressure and the organics were taken up in dichloromethane, washed with brine (2x), dried over Mg_2SO_4, filtered, and concentrated to dryness. HDPP-Pent was obtained as a blue solid by silica-column chromatography (3 : 1 Hexanes/CH_2Cl_2, followed by 5 : 1 Hexanes/THF, then 5:1:1 Hexanes/CH_2Cl_2/Toluene with 1% MeOH). ^{1}H NMR (400 MHz, CD_2Cl_2, 25 ºC): δ 10.39 (s, 1H), 8.48 (br s, 4H), 7.64 – 7.58 (m, 5H), 7.48 (d, 5H), 7.43 (br s, 4H), 7.07 (d, 2H), 6.95 (dd, J = 6.2, 2.1 Hz, 2H), 6.84 – 6.73 (m, 9H), 1.46 (br s, 42H). ^{13}C NMR (101 MHz, CD_2Cl_2, 25 ºC): δ 158.1, 149.7, 136.0, 135.8, 133.3, 130.7, 130.0, 129.6, 127.7, 127.2, 127.0, 125.0, 124.6, 124.5, 124.0, 123.6, 117.2, 116.9, 109.3, 105.4, 103.4, 19.3, 12.0.

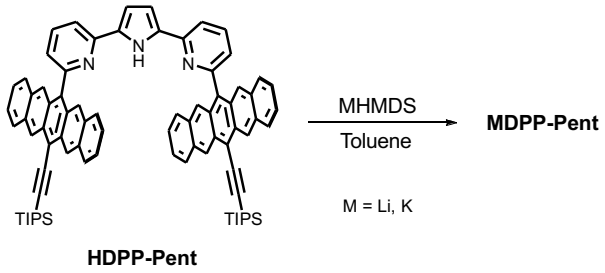

Figure S2. Synthetic scheme for MDPP-Pent (M = Li, K). HDPP-Pent is deprotonated with the appropriate alkali metal hexamethyldisilazide (MHMDS).

Synthesis of Li_2(DPP-Pent)$_2$

HDPP-Pent (0.1 mmol) was dissolved in toluene (3 mL) and a solution of lithium hexamethyldisilazide (0.1 mmol) in toluene (2 mL) was added and the mixture was stirred for 20 min. The solution quickly turned from blue to blue-green. Volatiles were removed via vacuum pressure and the desired product was obtained as a blue-green powder. ^{1}H NMR (400 MHz, CD_2Cl_2, 25 °C): δ 9.10 (s, 4H), δ 7.84 (d, 4H), δ 7.75 (s, 4H), δ 7.51 (d, 4H), δ 7.23 (dd, 4H), δ 6.93 (dd, 4H), δ 6.04 (m, 4H), δ 5.12 (d, 2H), δ 4.36 (s, 2H), δ 1.53 (m, 42H).

Synthesis of KDPP-Pent

HDPP-Pent (0.1 mmol) was dissolved in toluene (3 mL) and a solution of potassium hexamethyldisilazide (0.1 mmol) in toluene (2 mL) was added and the mixture was stirred for 20 min. The solution quickly turned from blue to blue-green. Volatiles were removed via vacuum pressure and the desired product was obtained as a blue-green powder. ^{1}H NMR (400 MHz, CD_2Cl_2, 25 °C): δ 9.13 (s, 4H), δ 8.15 (s, 4H), δ 7.80 (m, 8H), δ 7.59 (d, 4H), δ 7.24 (m, 4H), δ 7.15 (m, 4H), δ 7.01 (s, 2H), δ 6.96 (d, 2H), δ 1.35 (m, 42H).

III. 2D Rotating Frame Overhauser Effect Spectroscopy (ROESY)

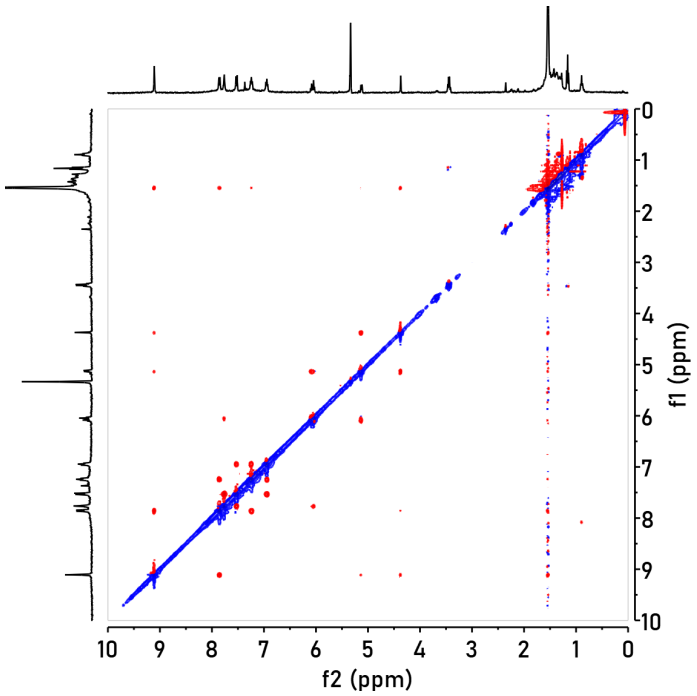

Figure S3. 2D ROESY spectrum of $Li_2(DPP\text{-}Pent)_2$ (400 MHz, CD_2Cl_2).

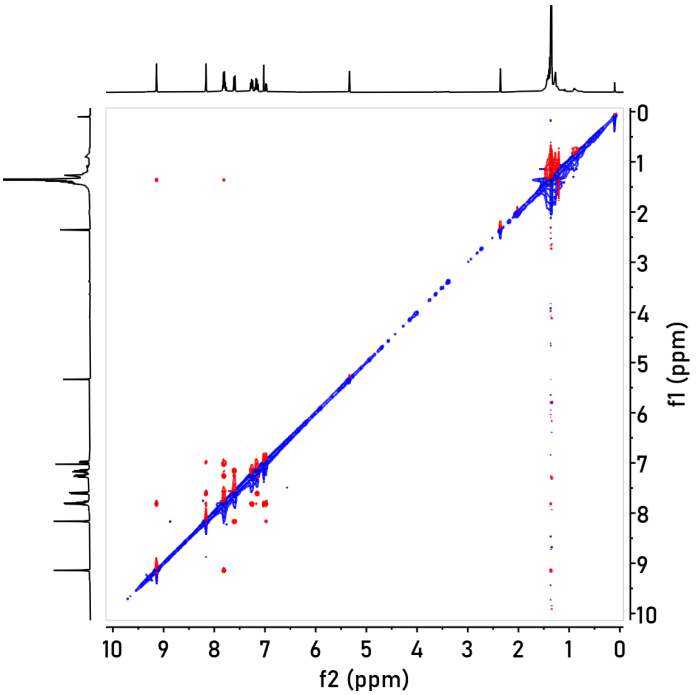

Figure S4. 2D ROESY spectrum of KDPP-Pent (400 MHz, CD_2Cl_2).

IV. Steady-state Absorption and Emission Spectroscopy

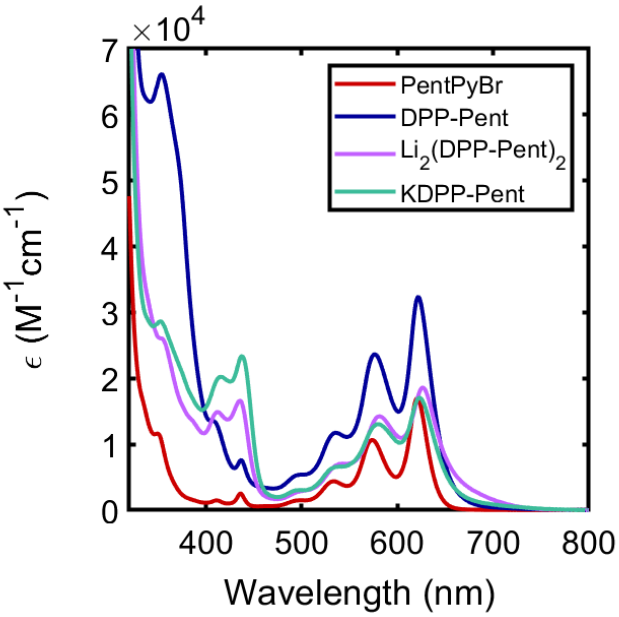

Figure S5. Visible absorption spectra of PentPyBr (red), HDPP-Pent (blue), $Li_2(DPP\text{-}Pent)_2$ (purple), and KDPP-Pent (teal) in toluene.

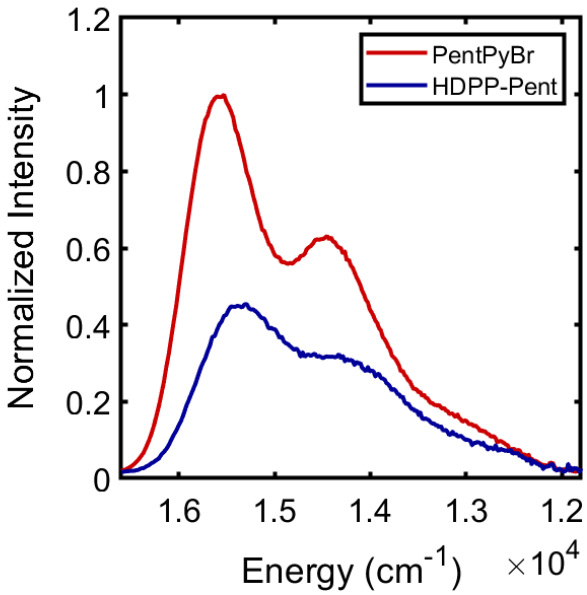

Figure S6. Emission spectra of PentPyBr (red) and HDPP-Pent (blue). The PentPyBr maximum signal intensity was normalized to one and the HDPP-Pent spectrum was scaled such that the integrated intensity of the samples reflected their relative estimated quantum yields.

V. Time-Resolved Luminescence Spectroscopy

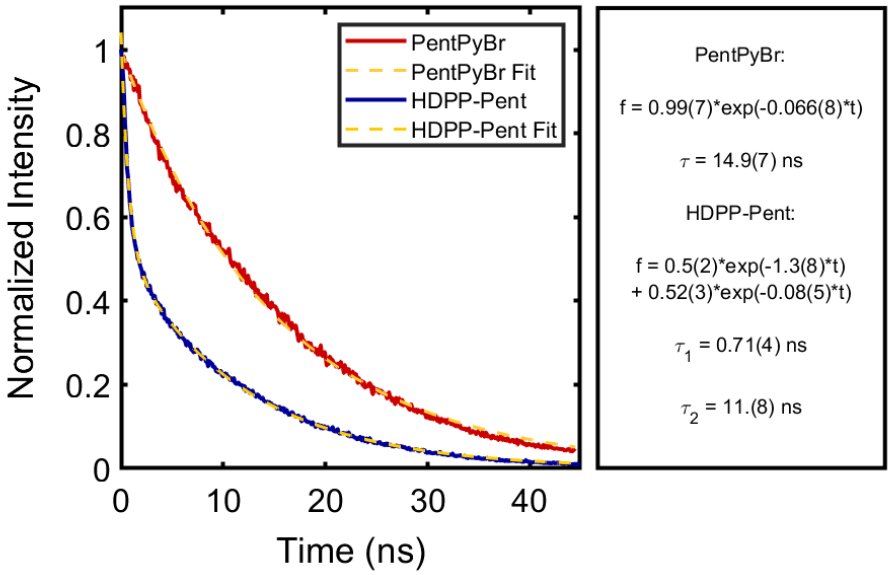

Figure S7. Time-resolved luminescence spectra of PentPyBr (λ_{obs} = 640 nm) and HDPP-Pent (λ_{obs} = 650 nm) after excitation at 532 nm. The spectra were normalized to a maximum of 1. The fluorescence decay of PentPyBr was fit to a monoexponential function (τ = 15 ns), whereas the decay of HDPP-Pent had to be fit biexponentially (τ_1 = 0.71 ns, τ_2 = 11.8 ns).

VI. Transient Absorption Spectroscopy

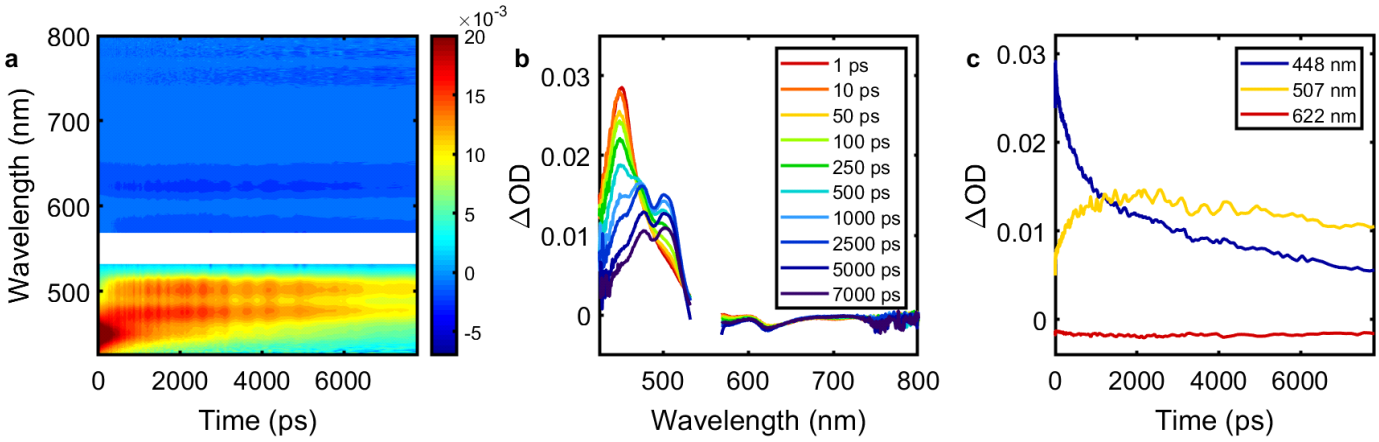

Figure S8. Femtosecond visible transient absorption spectra of HDPP-Pent (50 μM, toluene) after excitation at 550 nm (0.100 μJ/pulse): (a) contour plot, (b) spectral traces at various time delays, (c) selected time traces at 448, 507, and 622 nm.

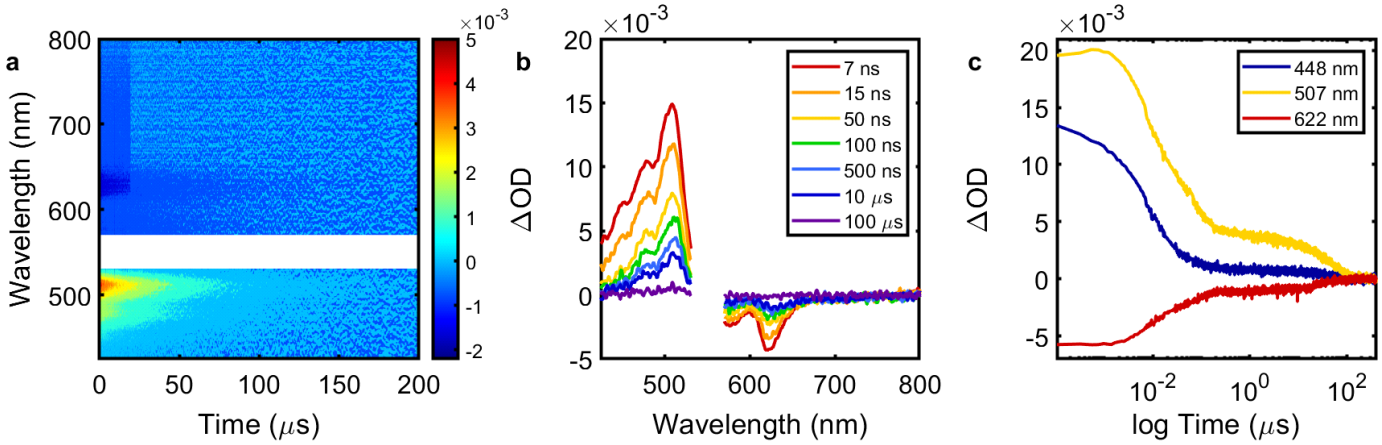

Figure S9. Nanosecond visible transient absorption spectra of HDPP-Pent (50 μM, toluene) after excitation at 550 nm (0.100 μJ/pulse): (a) contour plot, (b) spectral traces at various time delays, (c) selected time traces at 448, 507, and 622 nm.

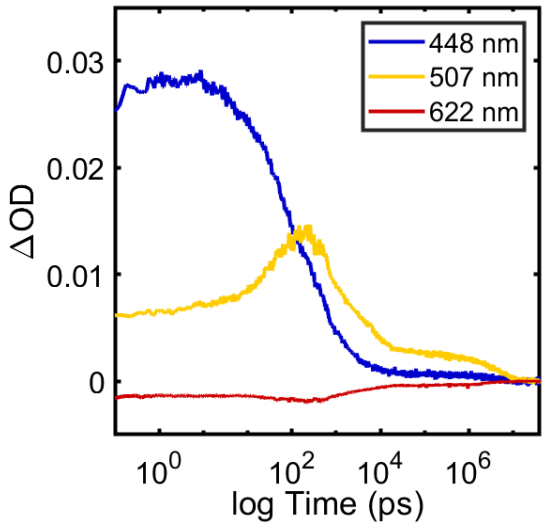

Figure S10. Combined visible fs and ns TA spectra of HDPP-Pent (50 μM, toluene) after excitation at 550 nm (0.100 μJ/pulse); time traces selected at 448, 507, and 622 nm.

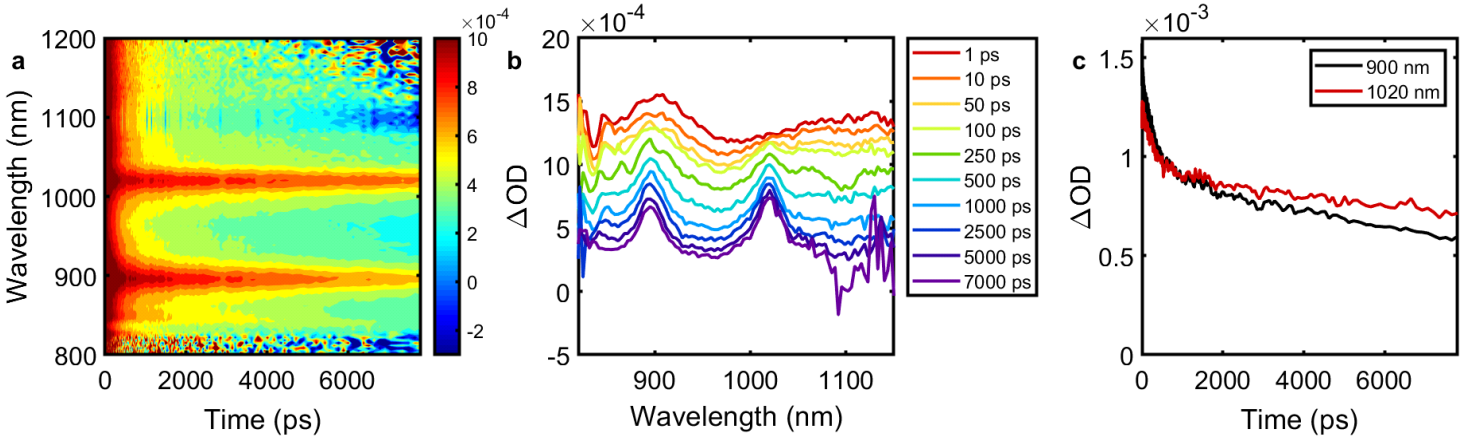

Figure S11. Near-IR fsTA spectra of HDPP-Pent (50 μM, toluene) after excitation at 550 nm (0.100 μJ/pulse): (a) contour plot, (b) spectral traces at various time delays, (c) selected time traces at 900 and 1020 nm.

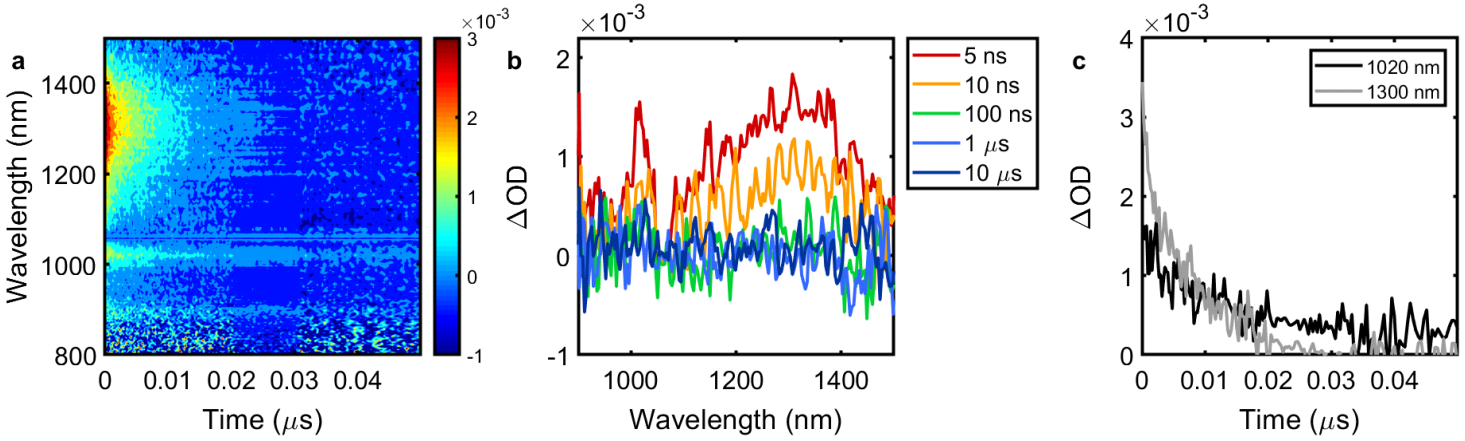

Figure S12. Near-IR nsTA spectra of HDPP-Pent (50 μM, toluene) after excitation at 550 nm (0.100 μJ/pulse): (a) contour plot, (b) spectral traces at various time delays, (c) selected time traces at 900 and 1020 nm.

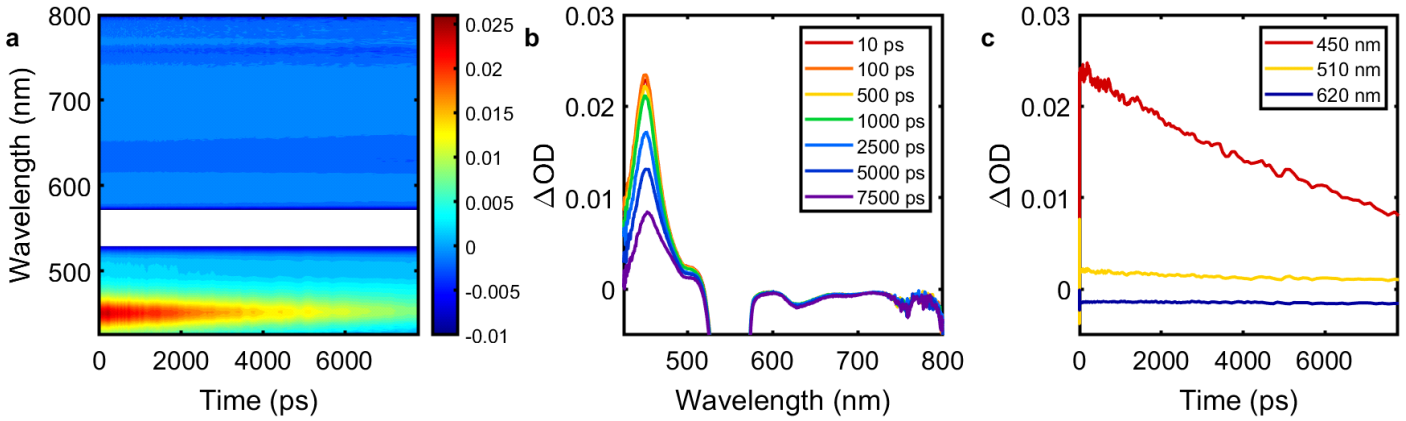

Figure S13. Visible fsTA spectra of PentPyBr (80 µM, toluene) after excitation at 550 nm (0.100 µJ/pulse): (a) contour plot, (b) spectral traces at various time delays, (c) selected time traces at 900 and 1020 nm.

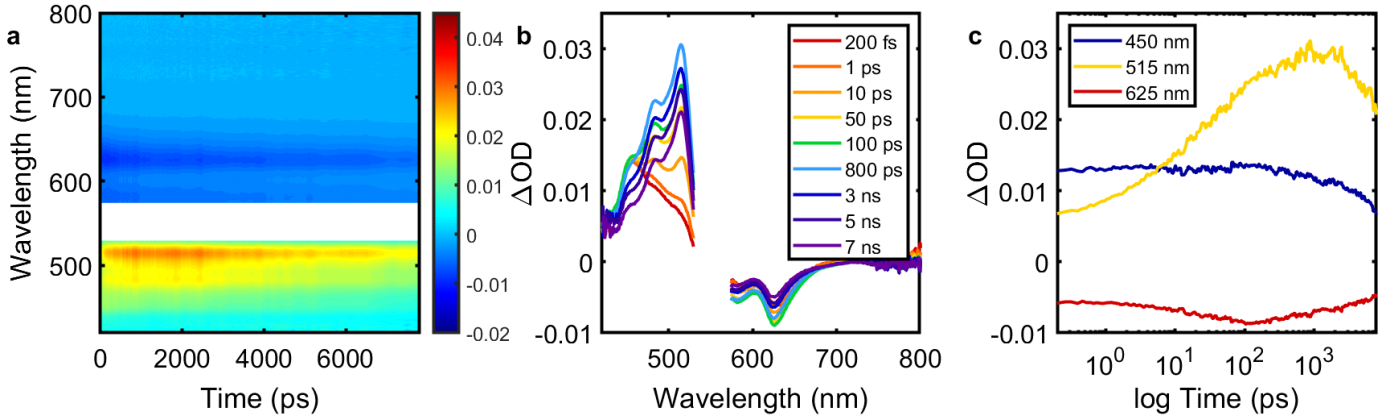

Figure S14. Visible fsTA spectra of Li_2(DPP-Pent)$_2$ (50 µM, toluene) after excitation at 550 nm (0.100 µJ/pulse): (a) contour plot, (b) spectral traces at various time delays, (c) selected time traces at 450, 515, and 625 nm.

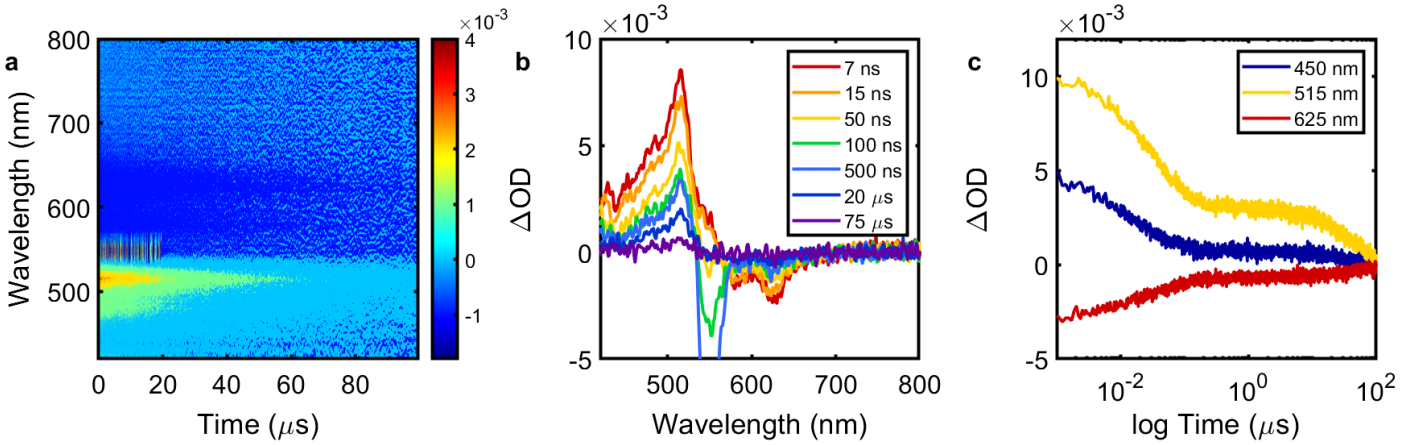

Figure S15. Visible nsTA spectra of Li_2(DPP-Pent)$_2$ (50 μM, toluene) after excitation at 550 nm (0.100 μJ/pulse): (a) contour plot, (b) spectral traces at various time delays, (c) selected time traces at 450, 515, and 625 nm.

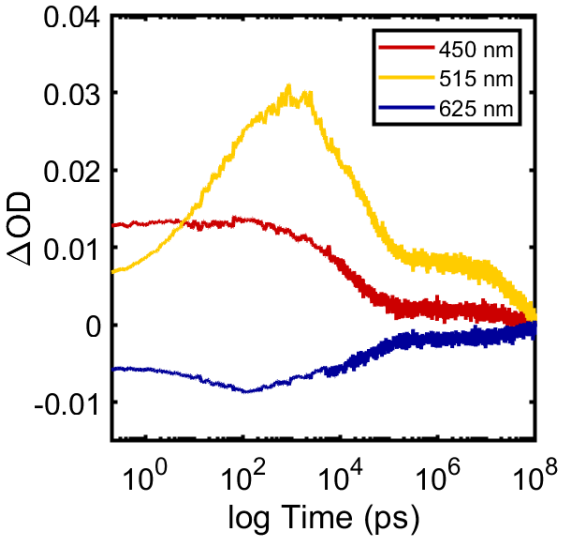

Figure S16. Combined visible fs and ns TA spectra of $Li_2(DPP\text{-}Pent)_2$ (50 μM, toluene) after excitation at 550 nm (0.100 μJ/pulse); time traces selected at 450, 515, and 625 nm.

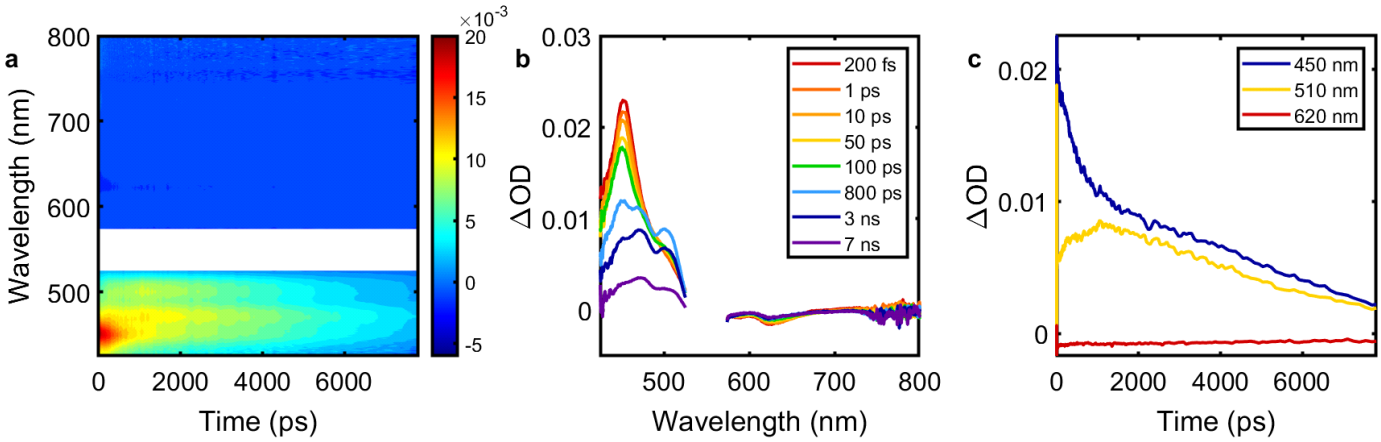

Figure S17. Visible fsTA spectra of KDPP-Pent (50 µM, toluene) after excitation at 550 nm (0.100 µJ/pulse): (a) contour plot, (b) spectral traces at various time delays, (c) selected time traces at 450, 510, and 620 nm.

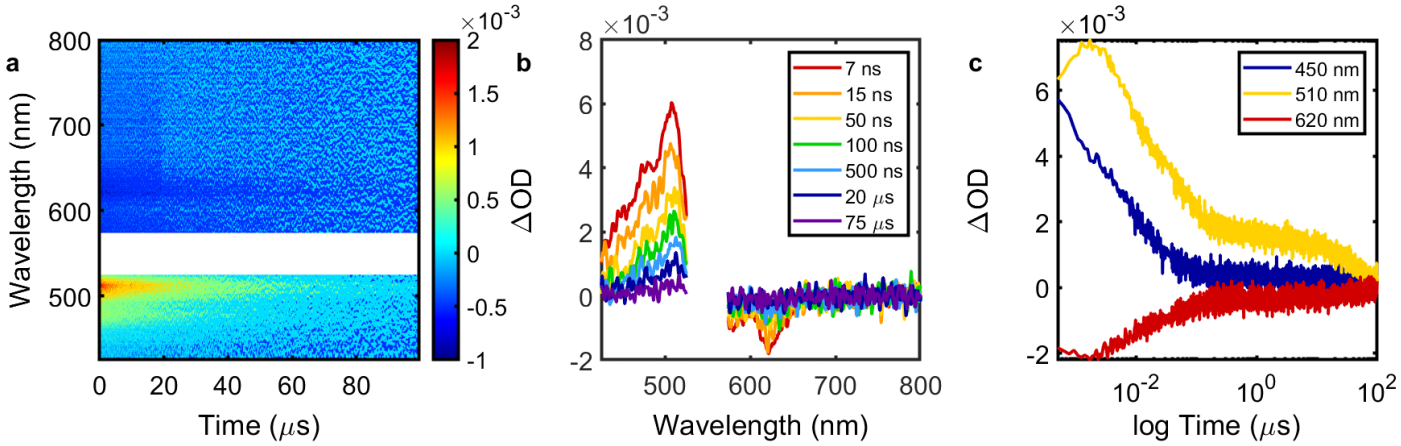

Figure S18. Visible nsTA spectra of KDPP-Pent (50 μM, toluene) after excitation at 550 nm (0.100 μJ/pulse): (a) contour plot, (b) spectral traces at various time delays, (c) selected time traces at 450, 510, and 620 nm.

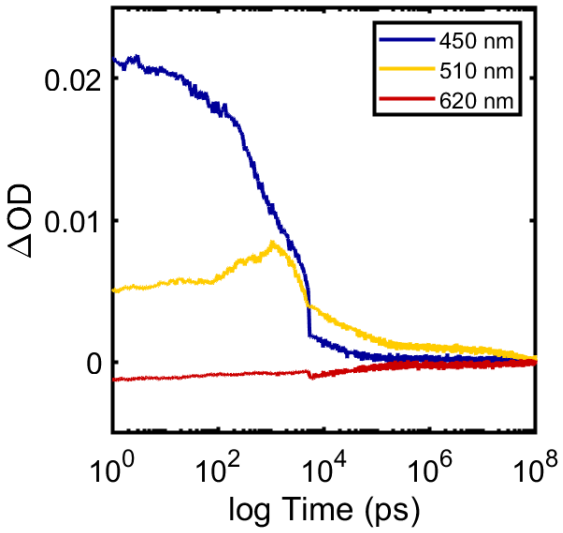

Figure S19. Combined visible fs and ns TA spectra of KDPP-Pent (50 μM, toluene) after excitation at 550 nm (0.100 μJ/pulse); time traces selected at 450, 510, and 620 nm.

VII. Target Kinetic Analysis

HDPP-Pent

For HDPP-Pent, the time-resolved luminescence data provide information solely on the dynamics of the S_1 state independent of the TA spectroscopy. The results of the emission experiment may therefore be appropriately applied to a kinetic model for fitting the composite TA data. Our model assumes the decay of the ^{1}ESA feature should mirror the biexponential decay observed in the time-resolved emission data, as both reflect the dynamics of the S_1 state. Thus, we require terms that account for both the radiative and nonradiative relaxation pathways. Initial attempts to fit single wavelength decay curves of the ^{3}ESA feature from the nsTA data to an exponential function clearly indicated the triplet decay required at least a biexponential. In fact, attempts to model the kinetics with only a monoexponential triplet decay produced results that exhibited significant intensity of the triplet feature in the singular value decomposition (SVD) of the residual data matrix, highlighting that the monoexponential decay model does not adequately describe the decay of the ^{3}ESA feature. This is consistent with other reports of multiexponential decays in the ^{3}ESA feature reflecting geminate recombination of the triplet pair on a faster timescale than un-correlated triplet decay.

In order to accommodate the biexponential decay of the ^{1}ESA, components 1 and 2 are set to equally reflect the ^{1}ESA spectrum and are weighted equally in initial intensity to reflect the weighting coefficients from the time-resolved fluorescence results (Supplementary Table S1). Components 3 and 4 are allowed to vary spectrally, but ultimately both reflect the ^{3}ESA feature. Component 1 decays into components 3 and 4 equally with a rate constant k_1, component 2 decays to the ground state with rate constant k_2, and components 3 and 4 decay to the ground state with rate constants k_3 and k_4 respectively.

Table S1. HDPP-Pent visible fs and ns TA target analysis; no parameters fixed

	k (s^{-1})	Standard Error
k_1	1.3(4) x 10^9	1.07 x 10^7
k_2	2.0(2) x 10^8	2.31 x 10^6
k_3	2.6(6) x 10^7	1.72 x 10^5
k_4	2.8(1) x 10^4	3.32 x 10^2

	t (ps)
t_1	7.4(6) x 10^2
t_2	4.9(5) x 10^3
t_3	3.7(6) x 10^4
t_4	3.5(6) x 10^7

	1	2	3	4
1				
2		k_2		
3	k_1		k_3	
4	k_1			k_4

Fitted kinetic parameters obtained from a four component model of the composite visible fs and ns TA data of HDPP-Pent: components 1 and 2 equally correspond to ^{1}ESA vectors (reflecting the biexponential decay observed from the time-resolved fluorescence measurements), components 3 and 4 similarly reflect the short- and long-lived ^{3}ESA vectors. Component 1 decays equally into components 3 and 4 with a rate k_1; components 2, 3, and 4 decay with a rate of k_2, k_3, k_4 respectively. Residual standard error 0.00175329.

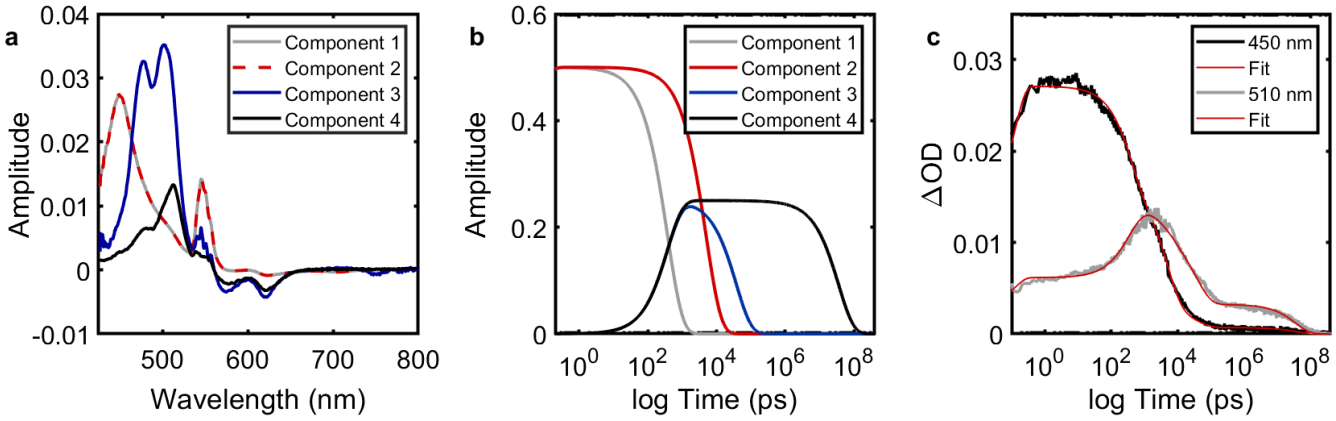

Figure S20. Glotaran target analysis (Table S1) of HDPP-Pent (50 μM, toluene) visible fs and ns TA data; no parameters fixed: (a) species associated spectra, (b) kinetic traces of fitted components, and (c) kinetic fits overlaying experimental data at 450 and 510 nm.

Table S2. HDPP-Pent visible fs and ns TA target analysis; k_1 and k_2 fixed

	k (s^{-1})	Standard Error
k_1	1.3(8) x 10^9	-
k_2	8.5(0) x 10^8	-
k_3	2.6(7) x 10^7	1.98 x 10^5
k_4	2.8(7) x 10^4	3.37 x 10^2
	t (ps)	
t_1	7.2(5) x 10^2	
t_2	1.1(8) x 10^4	
t_3	3.7(5) x 10^4	
t_4	3.4(8) x 10^7	

	1	2	3	4
1				
2		k_2		
3	k_1		k_3	
4	k_1			k_4

Fitted kinetic parameters obtained from a four component model of the composite visible fs and ns TA data of HDPP-Pent: components 1 and 2 equally correspond to ^{1}ESA vectors (reflecting the biexponential decay observed from the time-resolved fluorescence measurements), components 3 and 4 similarly reflect the short- and long-lived ^{3}ESA vectors. Component 1 decays equally into components 3 and 4 with a rate k_1; components 2, 3, and 4 decay with a rate of k_2, k_3, k_4 respectively. k_1 and k_2 have been fixed given the rates from time-resolved fluorescence measurements. Residual standard error: 0.00176051.

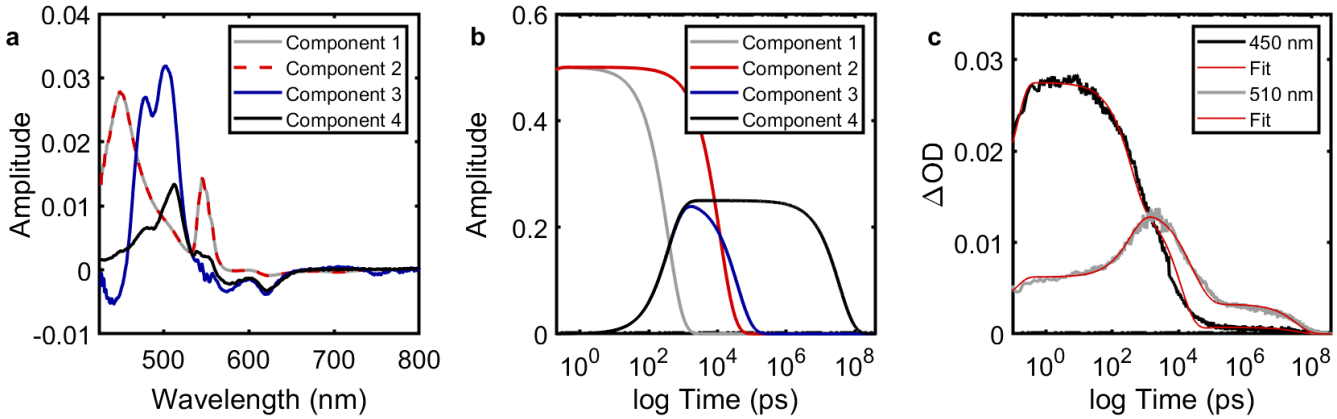

Figure S21. Glotaran target analysis (Table S2) of HDPP-Pent (50 µM, toluene) visible fs and ns TA data, k_1 and k_2 fixed: (a) species associated spectra, (b) kinetic traces of fitted components, and (c) kinetic fits overlaying experimental data at 450 and 510 nm.

Table S3. HDPP-Pent visible fsTA target analysis

	k (s^{-1})	Standard Error
k_1	2.5(6) x 10^9	3.86 x 10^7
k_2	1.7(2) x 10^8	5.20 x 10^6
k_3	1.(8) x 10^7	1.72 x 10^6
	t (ps)	
t_1	3.9(1) x 10^2	
t_2	5.8(1) x 10^3	
t_3	5.(6) x 10^4	

	1	2	3
1			
2		k_2	
3	k_1		k_3

Fitted kinetic parameters obtained from a three component model of the fsTA data of HDPP-Pent: components 1 and 2 equally correspond to ^{1}ESA vectors (reflecting the biexponential decay observed from the time-resolved fluorescence measurements), components 3 reflects the decay of the ^{3}ESA vector. Component 1 decays into component 3 with a rate k_1; components 2 and 3 decay with a rate of k_2 and k_3 respectively. Residual standard error: 0.00249052.

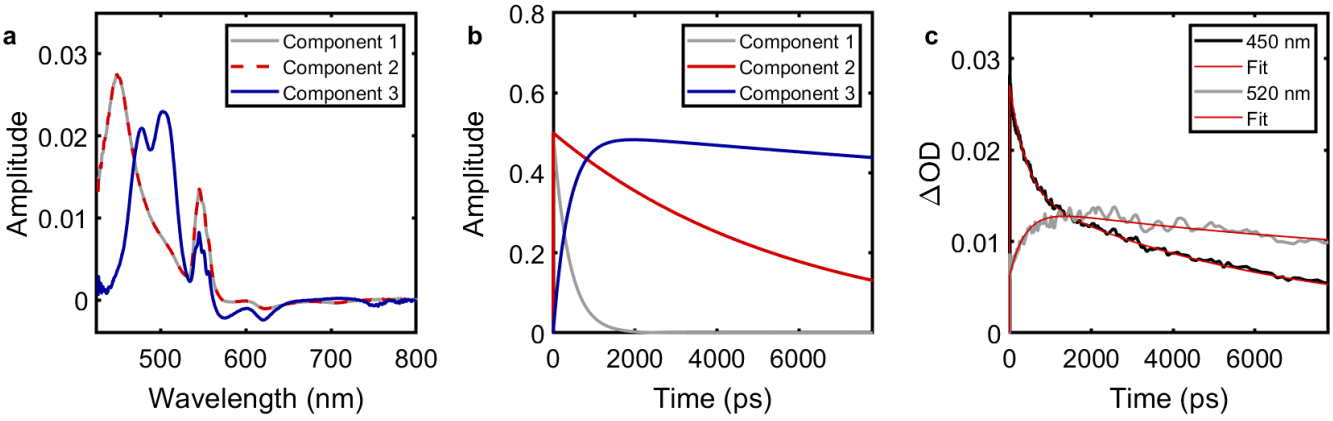

Figure S22. Glotaran target analysis (Table S3) of HDPP-Pent (50 µM, toluene) visible fsTA data: (a) species associated spectra, (b) kinetic traces of fitted components, and (c) kinetic fits overlaying experimental data at 450 and 510 nm.

Table S4. HDPP-Pent nsTA target analysis

	k (s^{-1})	Standard Error
k_1	3.5(5) x 10^7	1.76 x 10^5
k_2	2.9(4) x 10^4	2.74 x 10^2
	t (ns)	
t_1	2.8(2) x 10^1	
t_2	3.4(0) x 10^4	

	1	2
1	k_1	
2		k_2

Fitted kinetic parameters obtained from a three component model of the nsTA data of HDPP-Pent: components 1 and 2 correspond to ^{3}ESA vectors representing the biexponential decay in the feature. Components 1 and 2 decay with rate constants k_1 and k_2 respectively. Residual standard error: 0.00197139.

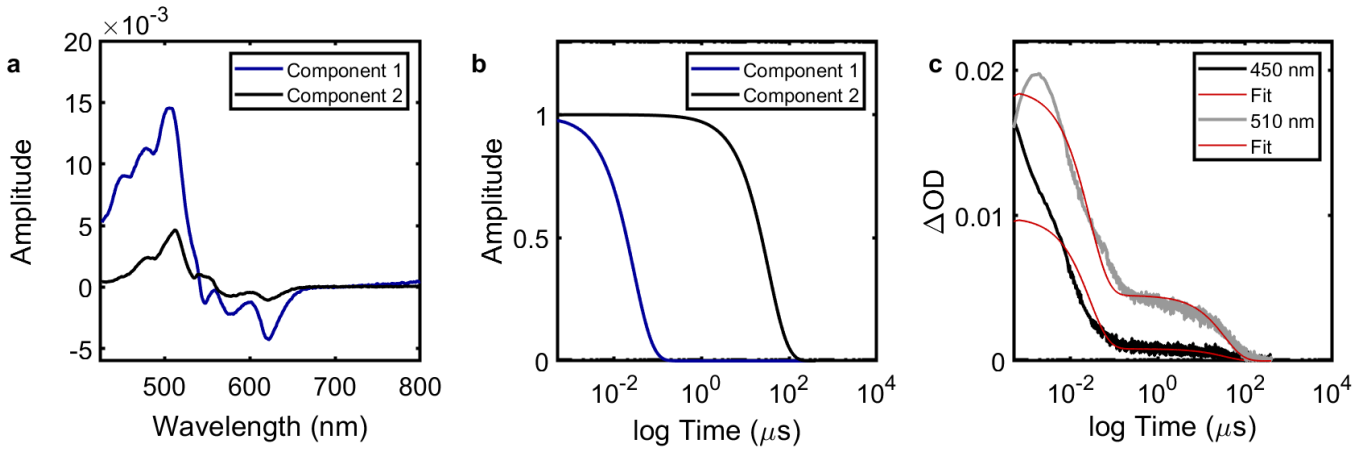

Figure S23. Glotaran target analysis (Table S4) of HDPP-Pent (50 μM, toluene) visible nsTA data: (a) species associated spectra, (b) kinetic traces of fitted components, and (c) kinetic fits overlaying experimental data at 450 and 510 nm.

Li_2(DPP-Pent)$_2$

Table S5. LiDPP-Pent visible fs and ns TA target analysis

	k (s^{-1})	Standard Error
k_1	7.2(2) x 10^9	4.04 x 10^7
k_2	3.98(3) x 10^7	9.309 x 10^4
k_3	2.3(8) x 10^4	1.00 x 10^2

	t (ps)
t_1	1.3(9) x 10^2
t_2	2.51(1) x 10^4
t_3	4.2(0) x 10^7

	1	2	3
1			
2	k_1	k_2	
3	k_1		k_3

Fitted kinetic parameters obtained from a three component model of the composite fs and ns TA data of Li_2(DPP-Pent)$_2$: component 1 corresponds to a ^{1}ESA, components 2 and 3 reflect the short- and long-lived ^{3}ESA vectors. Component 1 decays equally into components 2 and 3 with a rate k_1; components 2 and 3 decay with a rate of k_2 and k_3 respectively. Residual standard error 0.00181242.

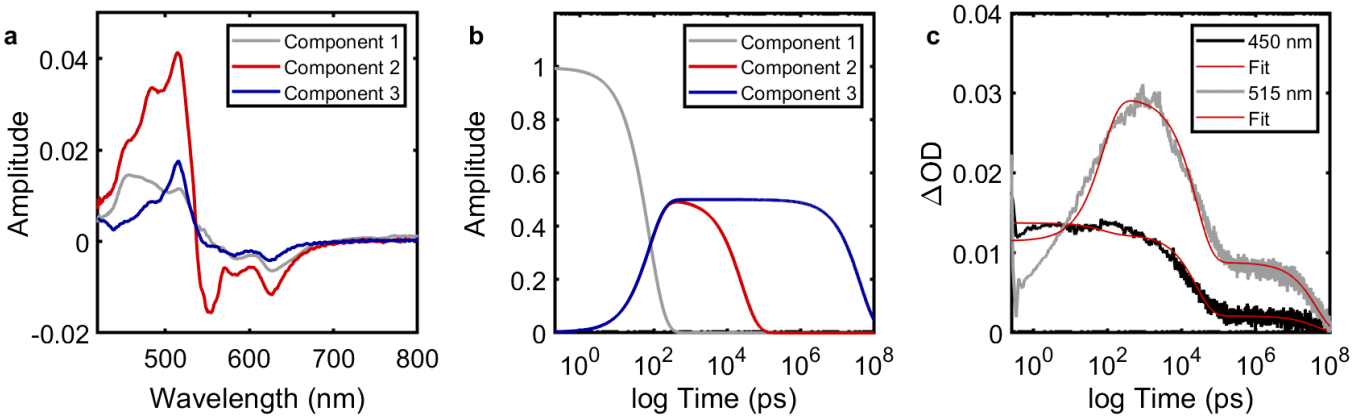

Figure S24. Glotaran target analysis (Table S5) of Li_2(DPP-Pent)$_2$ (50 µM, toluene) visible fs and ns TA data: (a) species associated spectra, (b) kinetic traces of fitted components, and (c) kinetic fits overlaying experimental data at 450 and 515 nm. The rapid rise of the triplet feature causes a slight deviation for the fits at these early times as seen in the intensity at 515 nm in the species associated spectra of component 1.

Table S6. $Li_2(DPP\text{-}Pent)_2$ visible fsTA target analysis

	k (s^{-1})	Standard Error
k_1	1.44(0) x 10^{10}	8.786 x 10^7
k_2	2.8(6) x 10^7	3.25 x 10^5
	t (ps)	
t_1	6.94(4) x 10^1	
t_2	2.51(1) x 10^4	

	1	2
1		
2	k_1	k_2

Fitted kinetic parameters obtained from a two-component, sequential model of the fsTA data of $Li_2(DPP\text{-}Pent)_2$: component 1 corresponds to a ^{1}ESA, and component 2 reflects the ^{3}ESA vector. Residual standard error 0.00211332.

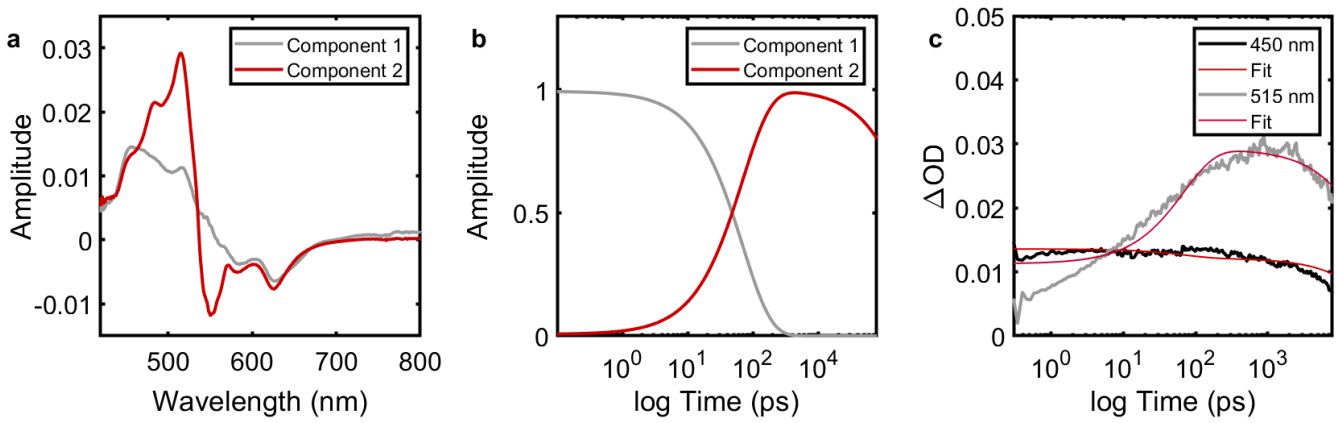

Figure S25. Glotaran target analysis (Table S6) of $Li_2(DPP\text{-}Pent)_2$ (50 µM, toluene) visible fsTA data: (a) evolution associated spectra, (b) kinetic traces of fitted components, and (c) kinetic fits overlaying experimental data at 450 and 510 nm. The rapid rise of the triplet feature causes a slight deviation for the fits at these early times as seen in the intensity at 515 nm in the species associated spectra of component 1.

Table S7. Li_2(DPP-Pent)$_2$ visible nsTA target analysis

	k (s^{-1})	Standard Error
k_1	2.60(2) x 10^7	7.978 x 10^4
k_2	2.19(1) x 10^4	9.291 x 10^1
	t (ns)	
t_1	3.84(3) x 10^1	
t_2	4.56(4) x 10^4	

	1	2
1	k_1	
2		k_2

Fitted kinetic parameters obtained from a two-component, sequential model of the nsTA data of Li_2(DPP-Pent)$_2$: components 1 and 2 correspond to the ^{3}ESA vector, reflecting a biexponential decay. Residual standard error 0.000664370.

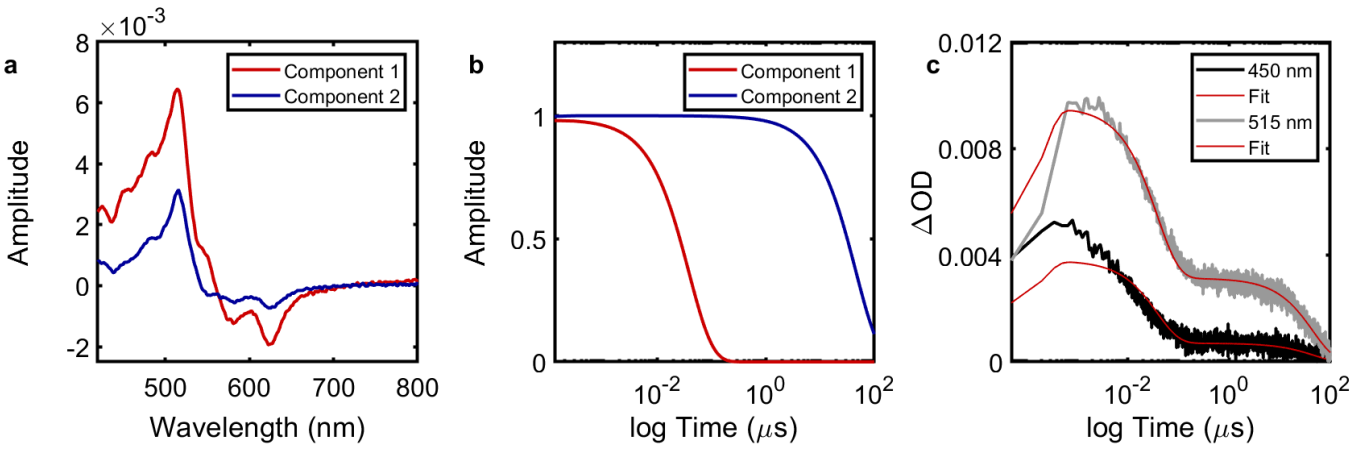

Figure S26. Glotaran target analysis (Table S7) of Li_2(DPP-Pent)$_2$ (50 μM, toluene) visible nsTA data: (a) species associated spectra, (b) kinetic traces of fitted components, and (c) kinetic fits overlaying experimental data at 450 and 510 nm.

KDPP-Pent

Table S8. KDPP-Pent visible fs and ns TA target analysis – 3 components

	k (s^{-1})	Standard Error
k_1	1.60(0) x 10^9	9.897 x 10^6
k_2	1.75(3) x 10^8	5.121 x 10^5
k_3	6.0(5) x 10^4	1.6(5) x 10^2

	t (ps)
t_1	6.25(0) x 10^2
t_2	5.70(5) x 10^4
t_3	1.6(5) x 10^7

	1	2	3
1			
2	k_1	k_2	
3	k_1		k_3

Fitted kinetic parameters obtained from a three component model of the composite fs and ns TA data of KDPP-Pent: component 1 corresponds to a ^{1}ESA, components 2 and 3 reflect the short- and long-lived ^{3}ESA vectors. Component 1 decays equally into components 2 and 3 with a rate k_1; components 2 and 3 decay with a rate of k_2 and k_3 respectively. Residual standard error 0.000864311.

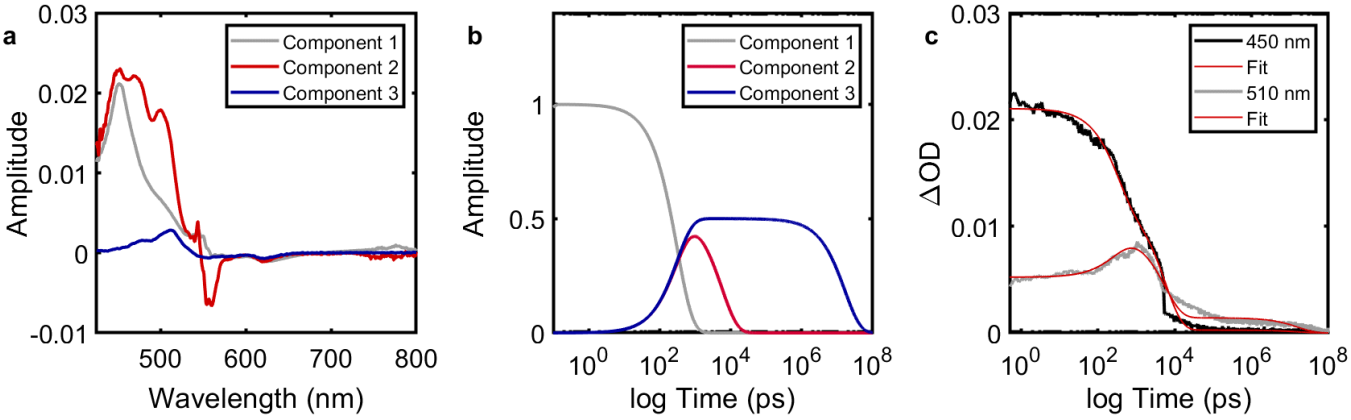

Figure S27. Glotaran target analysis (Table S8) of KDPP-Pent (50 µM, toluene) visible fs and nsTA data – 3 component fit: (a) species associated spectra, (b) kinetic traces of fitted components, and (c) kinetic fits overlaying experimental data at 450 and 510 nm.

Table S9. KDPP-Pent visible fs and ns TA target analysis – 4 components

	k (s^{-1})	Standard Error
k_1	2.2(5) x 10^9	1.71 x 10^7
k_2	2.7(5) x 10^8	2.14 x 10^6
k_3	8.7(1) x 10^7	4.85 x 10^5
k_4	3.7(2) x 10^4	4.85 x 10^2

	t (ps)
t_1	4.4(4) x 10^2
t_2	3.6(4) x 10^4
t_3	1.1(5) x 10^5
t_4	2.6(9) x 10^7

	1	2	3	4
1				
2		k_2		
3	k_1		k_3	
4	k_1			k_4

Fitted kinetic parameters obtained from a four component model of the composite fs and ns TA data of KDPP-Pent: components 1 and 2 equally correspond to ^{1}ESA vectors, components 3 and 4 similarly reflect the short- and long-lived ^{3}ESA vectors. Component 1 decays equally into components 3 and 4 with a rate k_1; components 2, 3, and 4 decay with a rate of k_2, k_3, k_4 respectively. Residual standard error 0.000862214. k_1 and k_2 have been fixed given the rates from time-resolved fluorescence measurements.

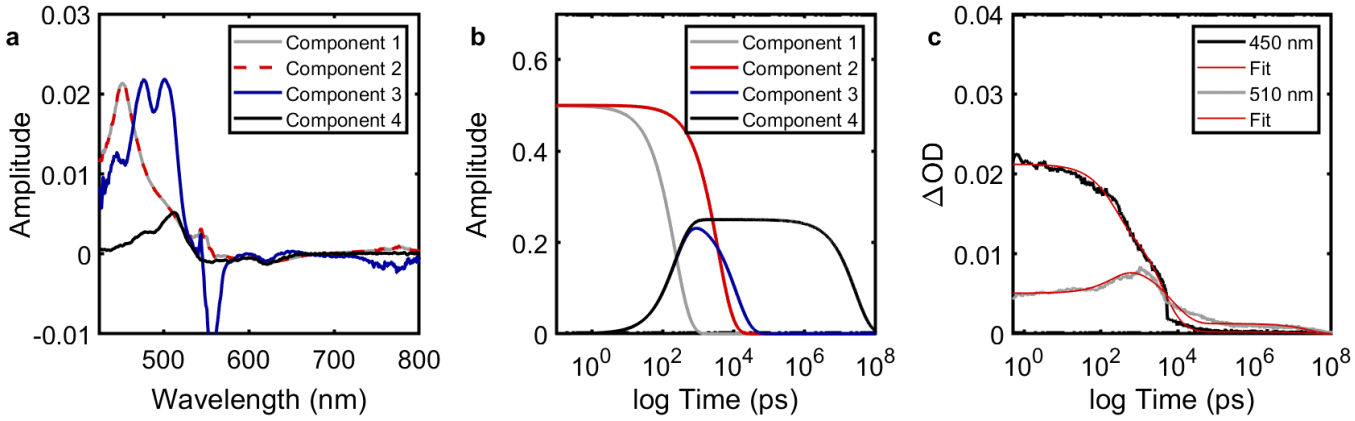

Figure S28. Glotaran target analysis (Table S9) of KDPP-Pent (50 µM, toluene) visible fs and nsTA data – four component fit: (a) species associated spectra, (b) kinetic traces of fitted components, and (c) kinetic fits overlaying experimental data at 450 and 510 nm.

Table S10. KDPP-Pent visible fsTA target analysis

	k (s^{-1})	Standard Error
k_1	2.2(7) x 10^9	2.86 x 10^7
k_2	1.4(4) x 10^8	1.14 x 10^6
	t (ps)	
t_1	4.4(1) x 10^2	
t_2	6.9(4) x 10^3	

	1	2
1		
2	k_1	k_2

Fitted kinetic parameters obtained from a two-component, sequential decay model of the fsTA data of KDPP-Pent: components 1 and 2 correspond to the ^{1}ESA and ^{3}ESA vectors, respectively. Residual standard error 0.00179745.

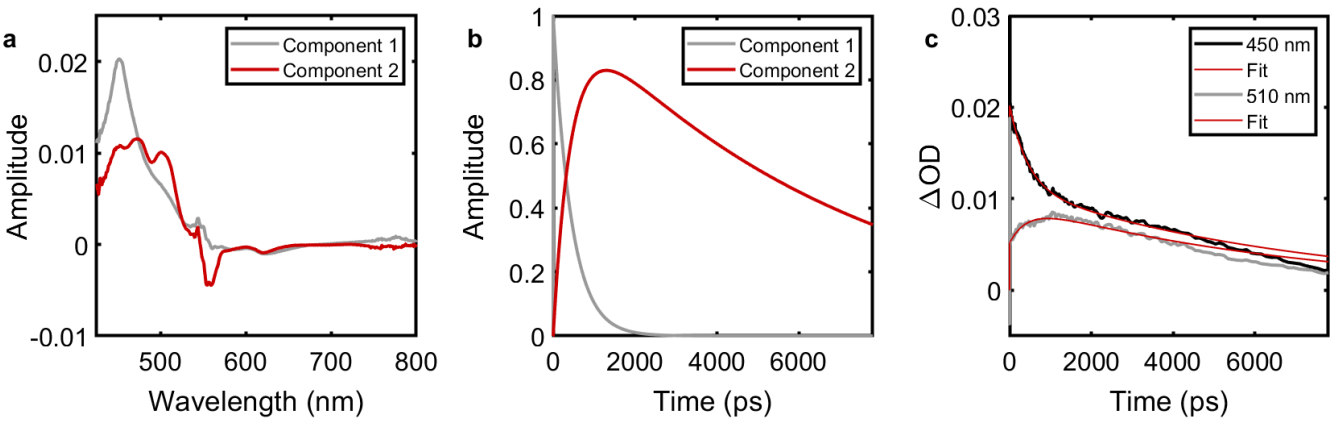

Figure S29. Glotaran target analysis (Table S10) of KDPP-Pent (50 µM, toluene) visible fsTA data: (a) evolution associated spectra, (b) kinetic traces of fitted components, and (c) kinetic fits overlaying experimental data at 450 and 510 nm.

Table S11. KDPP-Pent visible nsTA target analysis

	k (s^{-1})	Standard Error
k_1	3.1(6) x 10^7	1.27 x 10^5
k_2	2.7(3) x 10^4	1.14 x 10^2
	t (ns)	
t_1	3.1(6) x 10^1	
t_2	3.6(6) x 10^4	

	1	2
1	k_1	
2		k_2

Fitted kinetic parameters obtained from a two-component, parallel decay model of the nsTA data of KDPP-Pent: components 1 and 2 correspond to the ^{3}ESA vectors. Residual standard error 0.000674488.

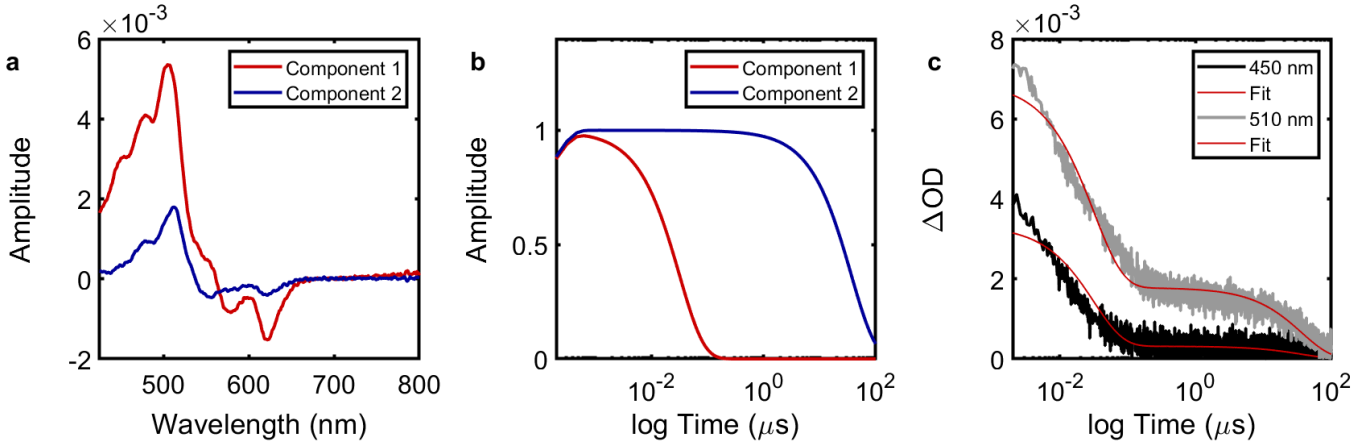

Figure S30. Glotaran target analysis (Table S11) of KDPP-Pent (50 μM, toluene) visible nsTA data: (a) evolution associated spectra, (b) kinetic traces of fitted components, and (c) kinetic fits overlaying experimental data at 450 and 510 nm.

VIII. HDPP-Pent: Triplet Extinction Coefficient Estimation

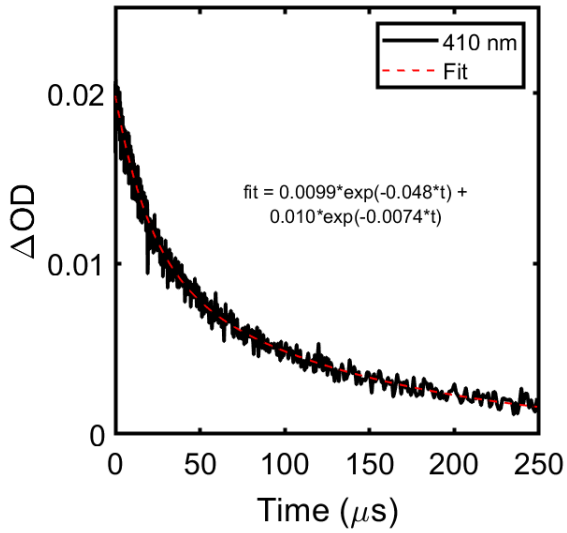

Figure S31. Anthracene (500 μM, toluene) ^{3}ESA ns transient absorption trace at 410 nm.

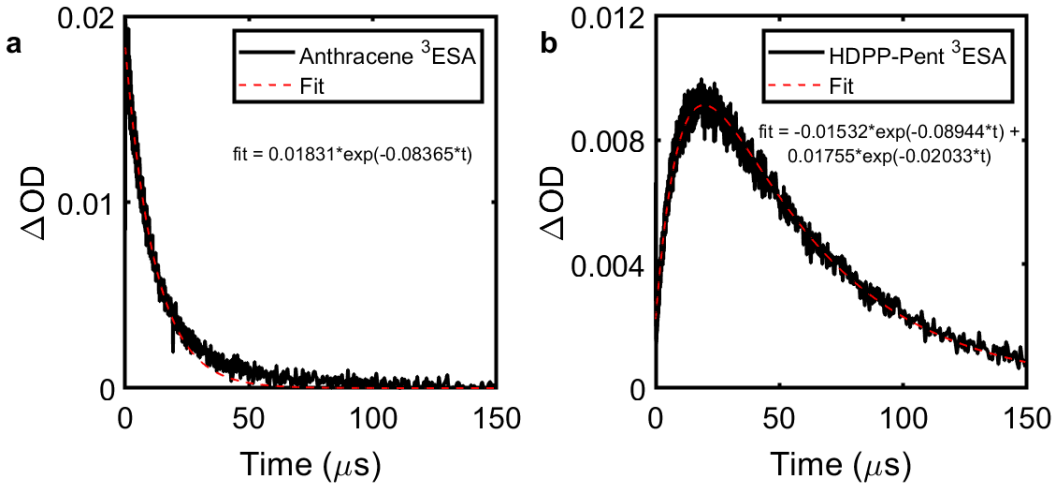

Figure S32. Photosensitization experiment (500 μM Anthracene, 10 μM HDPP-Pent in toluene): (a) Anthracene ^{3}ESA nsTA kinetic trace at 410 nm, (b) HDPP-Pent ^{3}ESA nsTA kinetic trace at 510 nm.

The Anthracene (500 μM) and HDPP-Pent (10 μM) photosensitization experiment will be used to demonstrate the calculation of the HDPP-Pent ^{3}ESA extinction coefficient given the reported Anthracene ^{3}ESA molar absorptivity (42,000 M^{-1} cm^{-1}).[4–7] This is accomplished by setting the concentrations of Anthracene and HDPP-Pent triplets to be equal in the Beer-Lambert regime and solving for ^{3}HDPP-Pent ε as in Equation 2:

$$c\,{}^3{}_{Anth} = c\,{}^3{}_{HDPP-Pent}$$

$$\frac{\Delta OD\,{}^3{}_{Anth}}{\varepsilon\,{}^3{}_{Anth} \cdot l} = \frac{\Delta OD\,{}^3{}_{HDPP-Pent}}{\varepsilon\,{}^3{}_{HDPP-Pent} \cdot l}$$

$$\varepsilon\,{}^3{}_{HDPP-Pent} = \frac{\Delta OD\,{}^3{}_{HDPP-Pent}}{\Delta OD\,{}^3{}_{Anth}} \cdot \varepsilon\,{}^3{}_{Anth} \qquad Eq\ (2)$$

The assumption underlying this equation is that the energy transfer efficiency is near unity – that the concentration of anthracene triplets fully transfers into HDPP-Pent triplets. In order to fulfill this estimation, corrections must be made to the ^{3} HDPP-Pent ΔOD to account for triplet

transfer efficiency (Φ_{ET}) and the relative rate of the rise and decay of the HDPP-Pent ^{3}ESA ($\Phi_{T(decay)}$).

$$\Phi_{ET} = \frac{k_{sens}}{k_{sens} + k_{intrinsic}}$$

$$\Phi_{ET} = \frac{0.08365}{0.08365 + 0.048} = 0.64$$

$$\Phi_{T(decay)} = \frac{k_{T(rise)}}{k_{T(rise)} + k_{T(decay)}}$$

$$\Phi_{T(decay)} = \frac{0.08944}{0.08944 + 0.02033} = 0.81$$

The corrected ^{3}HDPP-Pent ΔOD (ΔOD_{corr}) can thus be estimated and the HDPP-Pent ^{3}ESA extinction coefficient can be calculated as in Equation 2:

$$\Delta OD_{corr} = \frac{\Delta OD\ {}^3{}_{HDPP-Pent}}{\Phi_{ET} \cdot \Phi_{T(decay)}} = \frac{0.0091}{0.64 \cdot 0.81}$$

$$\Delta OD_{corr} = 0.0176$$

$$\varepsilon\ {}^3{}_{HDPP-Pent} = \frac{0.0176}{0.0183} \cdot (42{,}000\ M^{-1}cm^{-1})$$

$$\varepsilon\ {}^3{}_{HDPP-Pent} = 40{,}393\ M^{-1}cm^{-1}$$

This process is repeated for each concentration of HDPP-Pent (10, 20, 50, 100 μM) and the results are compiled in Figure S33. As can be seen, the calculated ^{3}HDPP-Pent extinction coefficient approaches a limit of ~ 49,000 M^{-1} cm^{-1} as the concentration of HDPP-Pent is increased (i.e. the triplet energy transfer efficiency approaches unity).

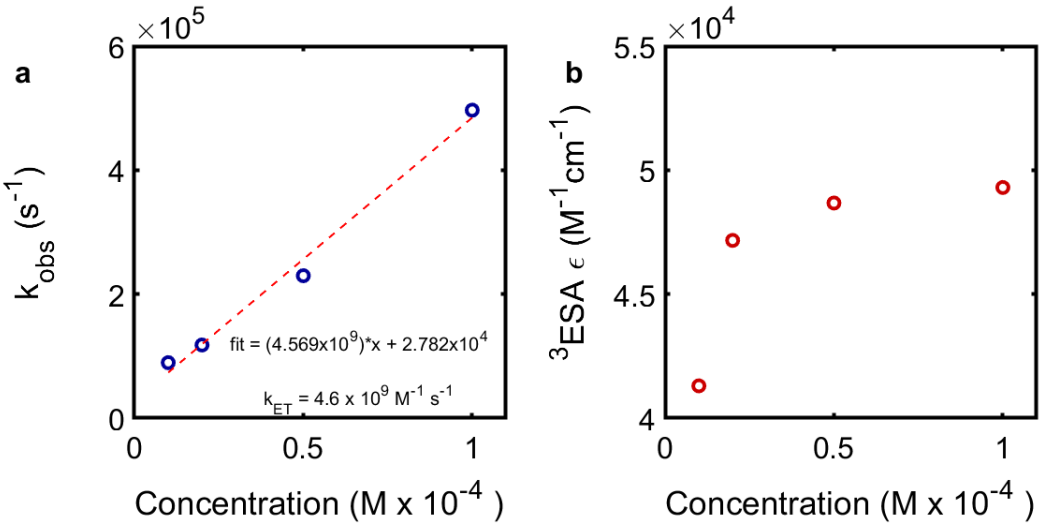

Figure S33. Concentration-dependent photosensitization experiments between Anthracene (500 μM) and HDPP-Pent (X μM, X = 10, 20, 50, 100): (a) observed energy transfer rate (k_{obs}) vs HDPP-Pent concentration, fitted to a linear function, the slope of which gives the bimolecular rate constant (k_{ET}); (b) calculated HDPP-Pent ^{3}ESA extinction coefficient vs HDPP-Pent concentration.

IX. HDPP-Pent: Triplet Yield Estimation

In order to estimate the triplet yield, we can use Equation 3. As a note, we refer to $[T_1]$ as the concentration of excited triplet states without differentiation between triplet pair (T_1T_1) and free triplet (T_1) states.

$$Triplet\ \%\ Yield = \frac{[T_1]}{[S_1]} \cdot 100 \qquad Eq\ (3)$$

i. Concentration of Excited Singlets

Let us first consider the maximum concentration of excited singlets generated. This has been previously estimated using the ground state bleach (GSB) feature. However, it must be noted in the case of HDPP-Pent that the shape and intensity of the GSB changes over the course of the transient absorption experiment in a way that suggests there is a complex overlap of GSB and ESA features in the spectrum. This makes the GSB unreliable in the evaluation of the triplet yield. The concentration of excited singlets may alternatively be estimated as the product of the number of photons per pulse and the ratio of pump intensity before and after the sample (I/I_0) divided by the product of Avogadro's number (N_A) and the excitation volume (V):[8]

$$[\boldsymbol{S_1}] = \frac{\left(\frac{\boldsymbol{photons}}{\boldsymbol{pulse}}\right) \cdot \left(\frac{\boldsymbol{I}}{\boldsymbol{I_0}}\right)}{\boldsymbol{N_A \cdot V}}$$

$$\left(\frac{photons}{pulse}\right) = \frac{power}{(rep\ rate) \cdot \left(\frac{energy}{photon}\right)}$$

$$\left(\frac{I}{I_0}\right) = 1 - 10^{-A}$$

$$V = \pi r^2 l$$

Each component may be first evaluated individually. The photons per pulse can be derived from the excitation power (100 μW), the laser repetition rate (1000 s^{-1}), and the energy per photon (as calculated by the product of Planck's constant h and the frequency of 550 nm light). I/I_0 can be calculated as the difference from unity of ten raised to the negative power of the sample absorbance at 550 nm (0.11). The excitation volume is assumed to be cylindrical using the radius of the excitation spot (0.013 cm) and the path length of the sample (0.2 cm).

$$\left(\frac{photons}{pulse}\right) = \frac{1 \times 10^{-4}\, W}{(1{,}000\, s^{-1}) \cdot (3.61 \times 10^{-19}\, J)} = 2.77 \times 10^{11}\, pulse^{-1}$$

$$\left(\frac{I}{I_0}\right) = 1 - 10^{-0.11} = 0.2238$$

$$V = \pi \cdot (1.30 \times 10^{-2}\, cm)^{2} \cdot (0.2\, cm) \cdot (0.001\, L\, cm^{-3}) = 1.06 \times 10^{-7}\, L$$

$$[S_1] = \frac{(2.77 \times 10^{11}) \cdot (0.2238)}{(6.022 \times 10^{23}) \cdot (1.06 \times 10^{-7})} = 9.7 \times 10^{-7}\, M$$

ii. Concentration of Excited Triplets

The concentration of HDPP-Pent triplets may be estimated from the extinction coefficient of the ^{3}ESA at 510 nm as derived above and the maximum ΔOD value at 510 nm from the experimental transient absorption data. However, from the time-resolved luminescence data and the target fitting, it is apparent that when the TA ^{3}ESA at 510 nm reaches its maximum intensity (t ~ 1.4 ns), there is contribution to this intensity from the ^{1}ESA. The fit may be used to decompose the ΔOD at 510 nm to its contributions from the ^{1}ESA and ^{3}ESA, and the triplet contribution may be used to estimate the corrected triplet yield.

The target fitting as shown in Figure S21 gives a maximum ΔOD_{510nm} of 0.0128. The contributions of the different component vectors to the target fit can be decomposed from the kinetic traces (Figure S21b), which provides a weighting coefficient or effective concentration for each vector at 1.4 ns. The SAS (Figure S21a) provide the relative molar extinction of each vector at 510 nm. Taking the weighted sum of the first and second vectors gives the ΔOD contribution of the ^{1}ESA at 510 nm. Likewise, taking the weighted sum of the third and fourth vectors gives the relative ΔOD contribution of the ^{3}ESA. These values are collected in Table S12.

Table S12. Estimation of ^{1}ESA and ^{3}ESA ΔOD contributions at 510 nm in the transient absorption spectrum of HDPP-Pent (50 μM, toluene).

component	1	2	3	4
Relative contribution at 1.4 ns	0.0103	0.4437	0.2379	0.2448
Intensity of SAS at 510 nm	0.0062	0.0062	0.0285	0.0180
	^{1}ESA		^{3}ESA	
?OD_{510nm} contribution at 1.4 ns	0.0028		0.010	

The maximum concentration of triplets can then be estimated in the Beer-Lambert regime and the triplet yield can be thus calculated.

$$[T_1] = \frac{\Delta OD_{510nm}}{\varepsilon\,{}^{3}{}_{DPP-Pent} \cdot l}$$

$$[T_1] = \frac{0.010}{(49{,}000) \cdot (0.2)} = 1.0 \times 10^{-6}\ M$$

$$Triplet\ Yield = \frac{[T_1]}{[S_1]} \cdot 100 = \frac{1.0 \times 10^{-6}\ M}{9.7 \times 10^{-7}\ M} \cdot 100$$

$$Triplet\ Yield \sim 100\ \%$$

X. Comparison of Singlet Fission Rates and Triplet Lifetimes

Table S13. Comparison between singlet fission (τ_{SF}) and triplet lifetimes (τ_T) for HDPP-Pent, Li_2(DPP-Pent)$_2$, KDPP-Pent, and previously reported bipentacene systems *ortho*-**2**, *meta*-**2**, and *para*-**2** (in benzonitrile),[9] BP0, BP1, BP2,[10] TFM, BCO, Spi, and EBD (in chloroform),[11] PD, and PT.[12] The compounds are referenced using the moniker given in their respective texts, and structures are provided for each following the table. Here, τ_T is used generally for the fitted lifetimes of the triplet features in the transient absorption spectrum, encompassing both ^{M}(TT) – the shorter lifetime(s) – and uncorrelated triplet lifetimes where applicable. A comprehensive review of lifetimes in covalently linked dimers appears in Korovina et al.[13]

	τ_{SF}	τ_T
ortho-**2**	500 fs	12 ps
meta-**2**	63 ps	2.2 ns
para-**2**	2.7 ps	17.3 ps
BP0	760 fs	450 ps
BP1	20 ps	16.5 ns
BP2	220 ps	270 ns (1)
TFM	49.7 ps	531 ns (1), 23.0 μs (2)
BCO	20 ns	1.8 μs (1), 18.0 μs (2)
Spi	54.5 ps	705 ns (1), 19.6 μs (2)
EBD	10.4 ps	174 ns (1), 24.3 μs (2)
PD	435 ps	8.3 ns (1); 87 ns (2); 25 μs (3)
PT	147 ps	12 ns (1); 70 ns (2); 32 μs (3)
HDPP-Pent	730 ps	36 ns (1); 35 μs (2)
Li_2(DPP-Pent)$_2$	140 ps	25 ns (1); 42 μs (2)
KDPP-Pent	400 – 600 ps	12 ns (1); 27 μs (2)

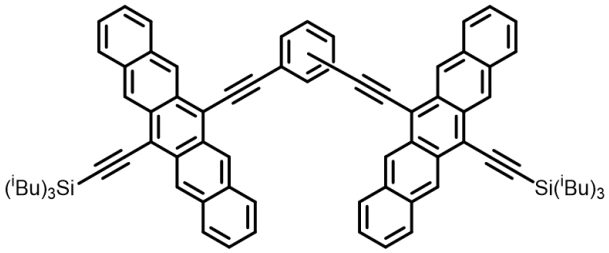

*ortho-, meta-, and para-***1**

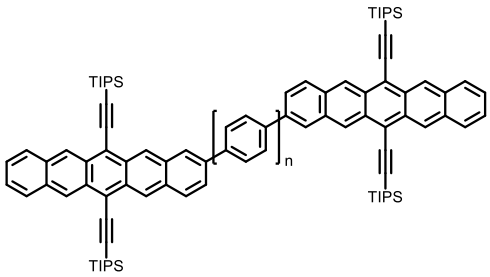

BPn (n=0,1,2)

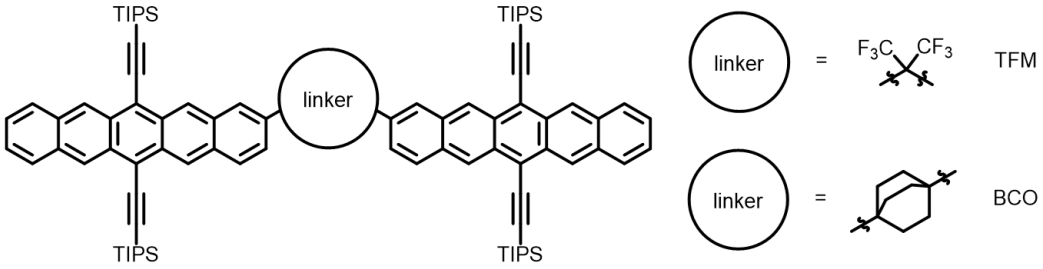

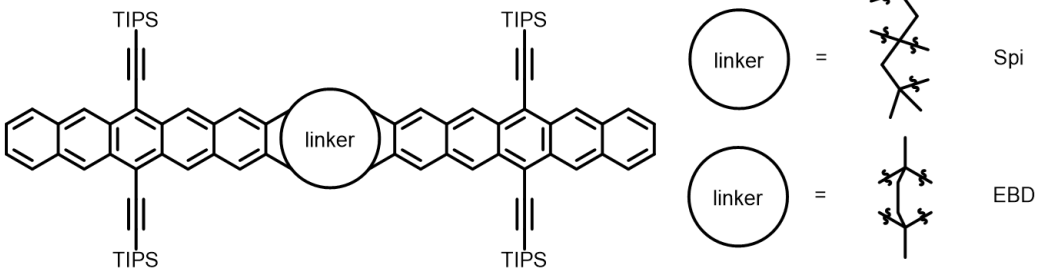

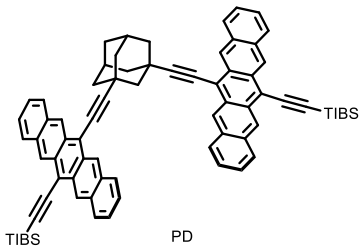

PD

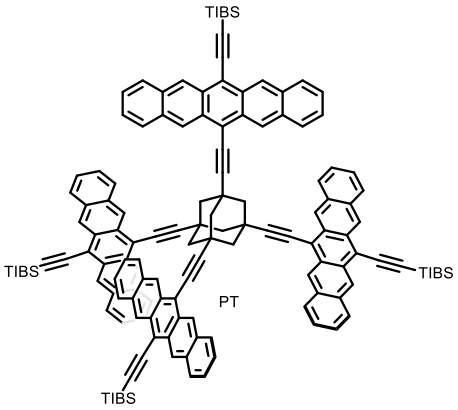

PT

XI. ^{1}H and ^{13}C NMR

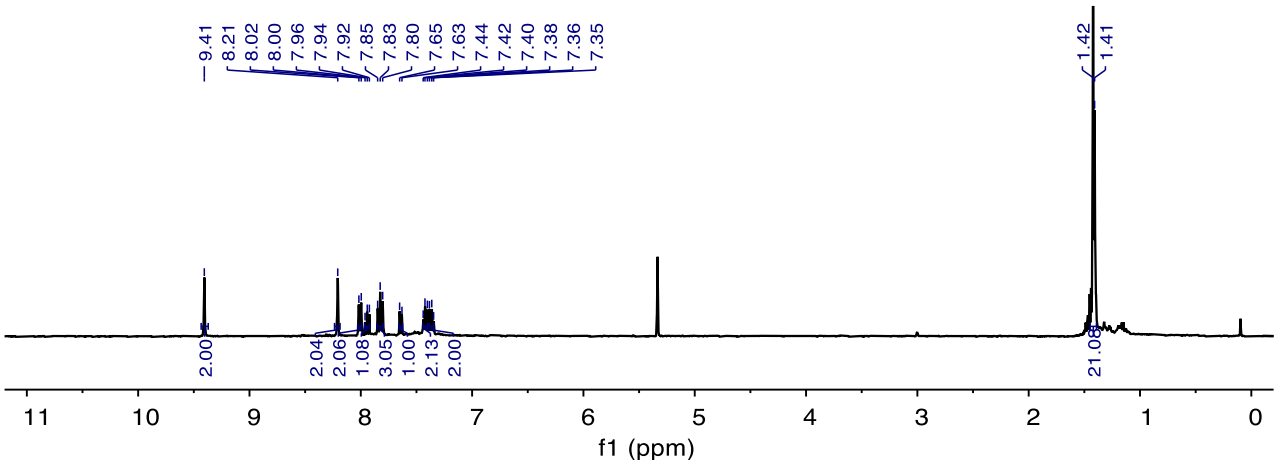

Figure S34. ^{1}H NMR spectrum of PentPyBr (400 MHz, $CDCl_3$).

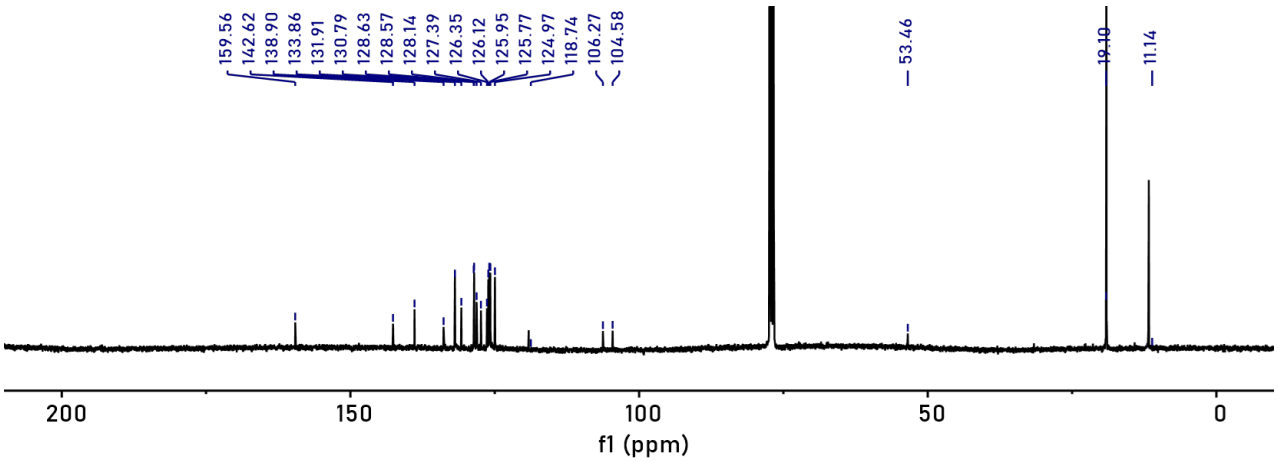

Figure S35. ^{13}C NMR spectrum of PentPyBr (400 MHz, $CDCl_3$).

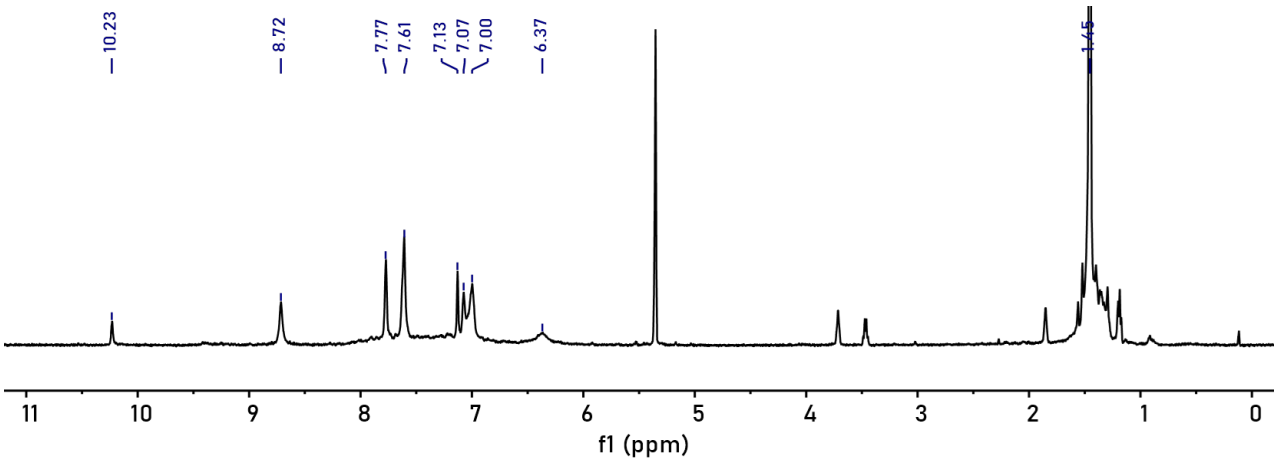

Figure S36. ^{1}H NMR spectrum of HDPP-Pent (400 MHz, CD_2Cl_2).

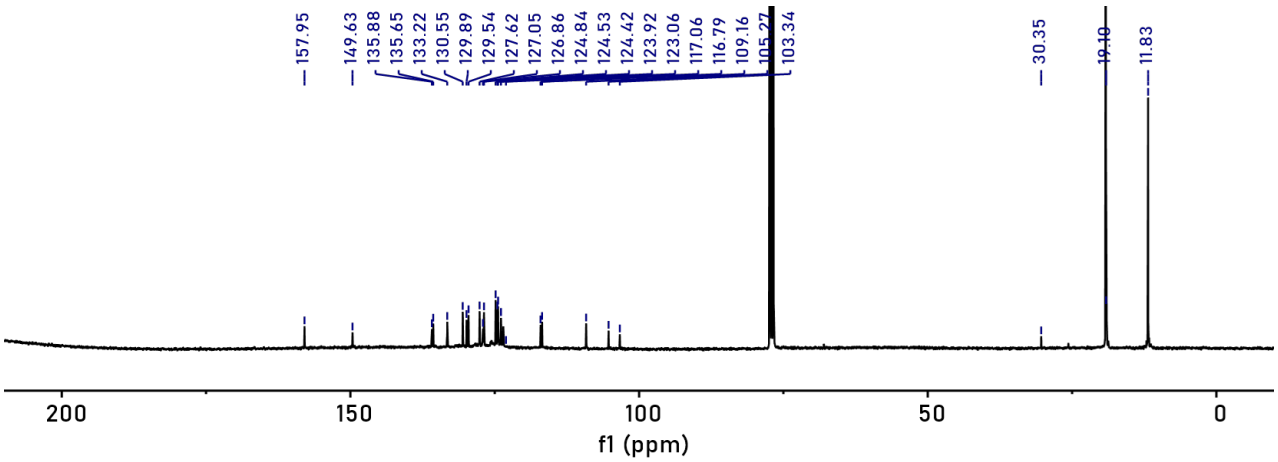

Figure S37. ^{13}C NMR spectrum of HDPP-Pent (400 MHz, $CDCl_3$).

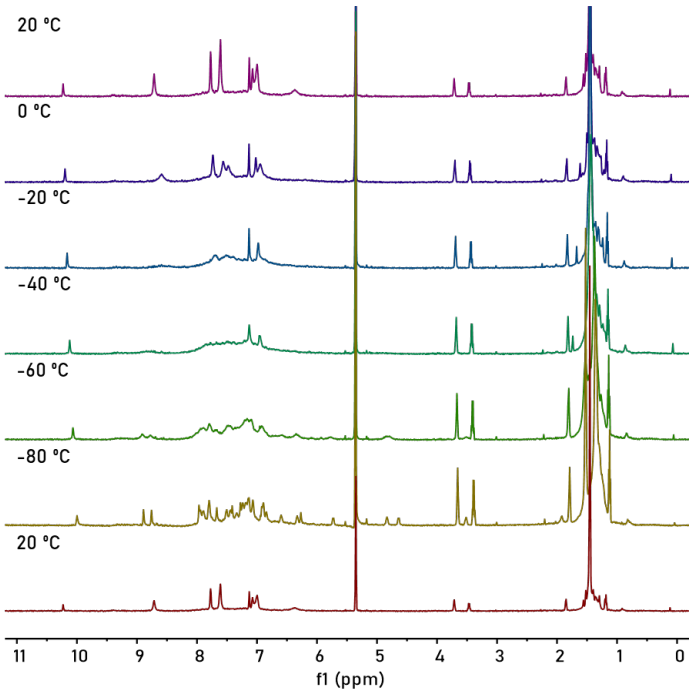

Figure S38. Variable temperature ^{1}H NMR spectra of HDPP-Pent (400 MHz, CD_2Cl_2).

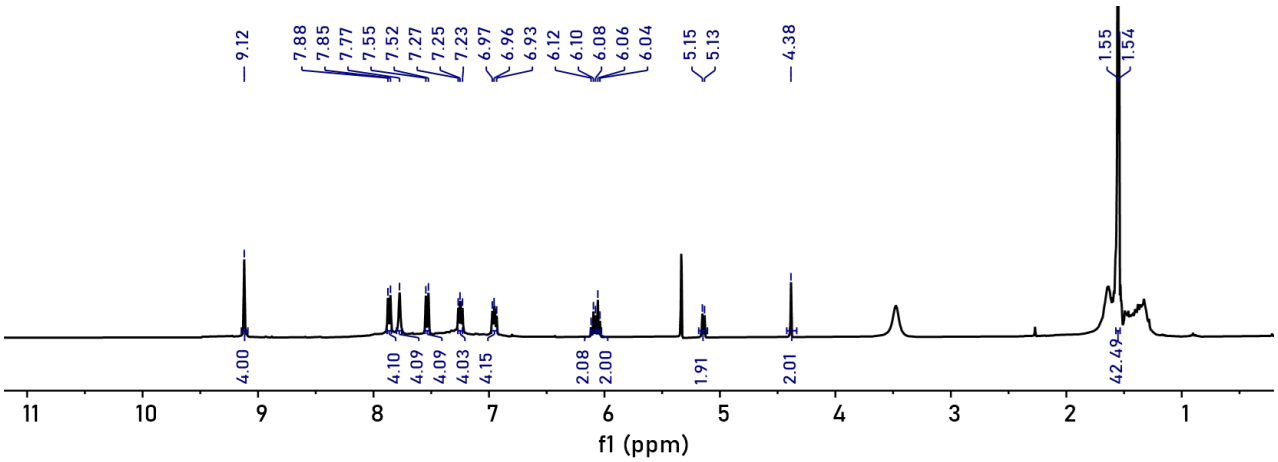

Figure S39. ^{1}H NMR spectrum of $Li_2(DPP\text{-}Pent)_2$ (400 MHz, CD_2Cl_2).

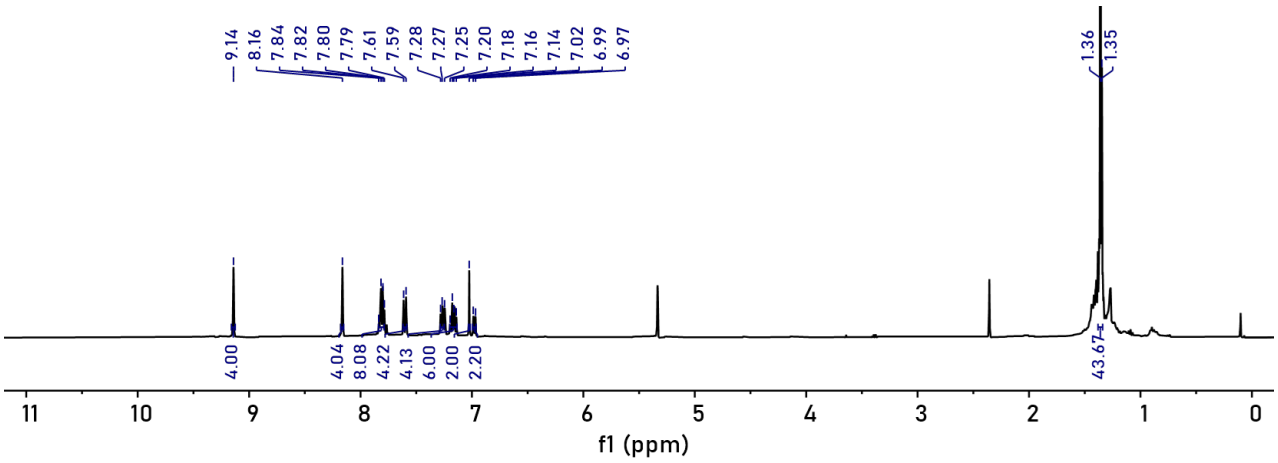

Figure S40. ^{1}H NMR spectrum of KDPP-Pent (400 MHz, CD_2Cl_2).

XII. $Li_2(DPP\text{-}Anth)_2$ Crystallographic Information

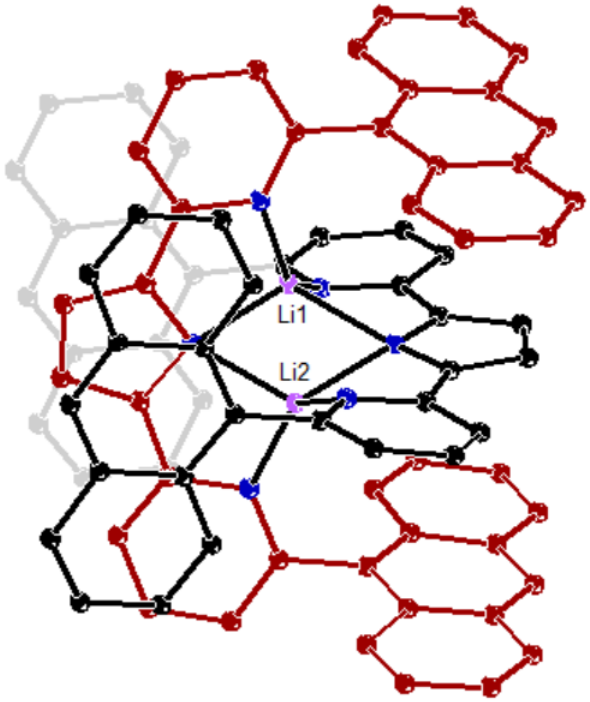

Figure S41. X-ray crystal structure of $Li_2(DPP\text{-}Anth)_2$. The DPP-Anth ligand 1 and 2 are coded as black and red, respectively. Ellipsoids are drawn at the 50% probability level.

1. Lehnherr, D., McDonald, R. & Tykwinski, R. R. Exploring Electronically Polarized Pentacenes. *Org. Lett.* **10**, 4163–4166 (2008).
2. Seechurn, C. C. C. J., Sivakumar, V., Satoskar, D. & Colacot, T. J. Iridium-Catalyzed C–H Borylation of Heterocycles Using an Overlooked 1,10-Phenanthroline Ligand: Reinventing the Catalytic Activity by Understanding the Solvent-Assisted Neutral to Cationic Switch. *Organometallics* **33**, 3514–3522 (2014).
3. Snellenburg, J. J., Laptenok, S., Seger, R., Mullen, K. M. & Stokkum, I. H. M. van. Glotaran: A Java-Based Graphical User Interface for the R Package TIMP. *Journal of Statistical Software* **49**, 1–22 (2012).
4. Bensasson, R. & Land, E. J. Triplet-triplet extinction coefficients via energy transfer. *Trans. Faraday Soc.* **67**, 1904–1915 (1971).
5. Amand, B. & Bensasson, R. Determination of triplet quantum yields by laser flash absorption spectroscopy. *Chemical Physics Letters* **34**, 44–48 (1975).
6. Compton, R. H., Grattan, K. T. V. & Morrow, T. Extinction coefficients and quantum yields for triplet—triplet absorption using laser flash photolysis. *Journal of Photochemistry* **14**, 61–66 (1980).
7. Nielsen, B. R., Jørgensen, K. & Skibsted, L. H. Triplet—triplet extinction coefficients, rate constants of triplet decay and rate constant of anthracene triplet sensitization by laser flash photolysis of astaxanthin, β-carotene, canthaxanthin and zeaxanthin in deaerated toluene at 298 K. *Journal of Photochemistry and Photobiology A: Chemistry* **112**, 127–133 (1998).
8. Walker, B. J., Musser, A. J., Beljonne, D. & Friend, R. H. Singlet exciton fission in solution. *Nature Chemistry* **5**, 1019–1024 (2013).
9. Zirzlmeier, J. *et al.* Singlet fission in pentacene dimers. *PNAS* **112**, 5325–5330 (2015).

10. Sanders, S. N. *et al.* Quantitative Intramolecular Singlet Fission in Bipentacenes. *J. Am. Chem. Soc.* **137**, 8965–8972 (2015).
11. Kumarasamy, E. *et al.* Tuning Singlet Fission in π-Bridge-π Chromophores. *J. Am. Chem. Soc.* **139**, 12488–12494 (2017).
12. Hetzer, C. *et al.* Chromophore Multiplication To Enable Exciton Delocalization and Triplet Diffusion Following Singlet Fission in Tetrameric Pentacene. *Angewandte Chemie International Edition* **58**, 15263–15267 (2019).
13. Korovina, N. V., Pompetti, N. F. & Johnson, J. C. Lessons from intramolecular singlet fission with covalently bound chromophores. *J. Chem. Phys.* **152**, 040904 (2020).